CHALMERS
UNIVERSITY OF TECHNOLOGY

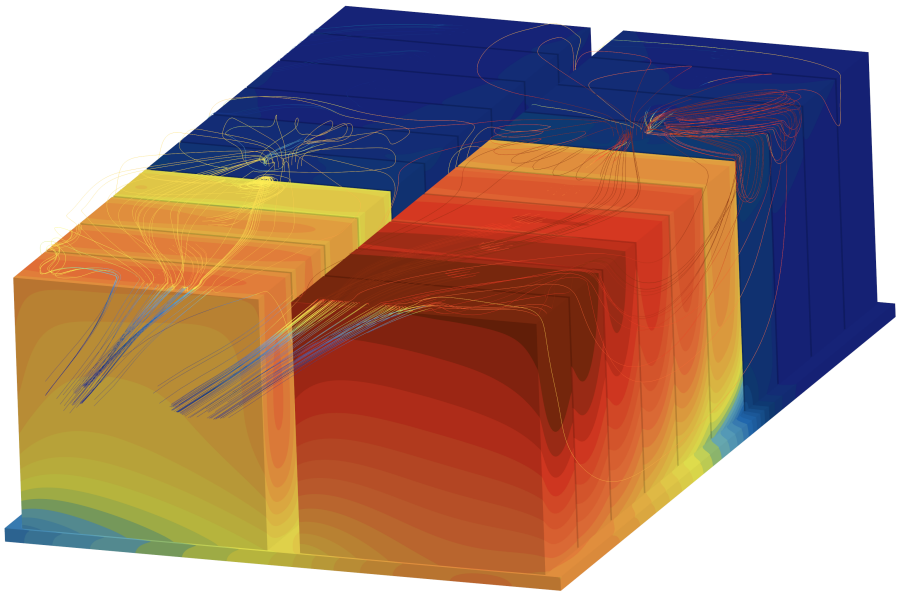

CFD study of Thermal Runaway in a Battery Module

Master's thesis in Applied Mechanics

Eric Lindblad

DEPARTMENT OF MECHANICS AND MARITIME SCIENCES

CHALMERS UNIVERSITY OF TECHNOLOGY
Gothenburg, Sweden 2024
www.chalmers.se

Master's thesis 2024

CFD study of Thermal Runaway in a Battery Module

Eric Lindblad

CHALMERS
UNIVERSITY OF TECHNOLOGY

Department of Mechanics and Maritime Sciences
Division of Fluid Dynamics
Chalmers University of Technology
Gothenburg, Sweden 2024

CFD study of Thermal Runaway in a Battery Module

Eric Lindblad

Supervisor: Robert Rundqvist, FS Dynamics
Examiner: Lars Davidson, Chalmers University of Technology

Master's Thesis 2024
Department of Mechanics and Maritime Sciences
Division of Fluid Dynamics
Chalmers University of Technology
SE-412 96 Gothenburg
Telephone +46 31 772 1000

Cover: Temperature contour of battery cell and cooling plate surface with streamlines visualizing the flow of gas from the vents.

Typeset in LaTeX
Printed by Chalmers Reproservice
Gothenburg, Sweden 2024

CFD study of Thermal Runaway in a Battery Module
Eric Lindblad
Department of Mechanics and Maritime Sciences
Chalmers University of Technology

Abstract

To fight climate change and decrease emissions battery powered electric vehicles are becoming more common. These vehicles often use lithium-ion batteries which if subject to extreme conditions can enter thermal runaway, a violent exothermic reaction that spreads between battery cells releasing energy in the form of heat and gases. This poses serious safety risks for the occupants of the vehicle and is something automotive manufacturers are trying to find ways to mitigate.

In this thesis thermal runaway is simulated using computational fluid dynamics to predict the propagation time between battery cells within a battery module. The commercial software Star-CCM+ was used to perform the simulations which included both built in and user created methods for capturing the behaviour of thermal runaway. After results for a baseline case were obtained two different mitigation strategies were implemented, one with cooling and one with improved insulation between the battery cells.

It was found that the methods used is this thesis can be implemented to simulate thermal runaway and to predict its propagation. A large portion of the heat released from each battery cell during thermal runaway was observed to be transported into the cooling plate, increasing the temperature of the neighboring cells. The hot gases released spread all throughout the battery module transferring heat to all battery cells. The mitigation strategies were both found to delay the propagation of thermal runaway with cooling being more effective delaying thermal runaway in the last battery cell by 18 seconds.

Keywords: CFD, Thermal Runaway, Battery, Lithium-ion, Turbulence modelling, Heat transfer, Star-CCM+

Acknowledgements

I would like to express my gratitude to everyone that has helped and supported me in some way during this project. At FS Dynamics I would first and foremost like to thank my supervisor Robert Rundqvist for his helpful guidance and feedback during the project. I also want to give a special thanks to Jakob Fredriksson and Jian Tan for being part of the weekly meetings and keeping the project on the right path. Last but not least I want to thank all colleagues at FS Dynamics for all help and support, big and small. I appreciate it very much.

At the Department of Mechanical and Maritime Sciences at Chalmers University of Technology I want to thank Lars Davidson for being the examiner of this master thesis.

Finally I want to thank my friends and family for always supporting and believing in me.

Eric Lindblad, Gothenburg, June 2024

List of Acronyms

Below is the list of acronyms that have been used throughout this thesis listed in alphabetical order:

CAD	Computer Aided Design
CFD	Computational Fluid Dynamics
DES	Detached Eddy Simulations
DNS	Direct Numerical Simulations
FVM	Finite Volume Method
ISC	Internal Short Circuit
LCO	Lithium Cobalt Oxide
LES	Large Eddy Simulations
LFP	Lithium Iron Phosphate
LIB	Lithium Ion Battery
RANS	Reynolds Averaged Navier-Stokes
SEI	Solid Electrolyte Interface
SST	Shear Stress Transport
TR	Thermal Runaway

Nomenclature

Below is the nomenclature of symbols, subscripts and superscripts that have been used throughout this thesis.

Symbols

ρ	Density (kg/m^3)
m	Mass (kg)
t	Time (s)
v	Velocity (m/s)
x	Spacial coordinate (m)
σ_{ij}	Stress tensor (Pa)
f_i	Volume force vector (N/kg)
δ_{ij}	Kronecker delta (-)
τ_{ij}	Viscous stress tensor (Pa)
μ	Dynamic viscosity (Pa·s)
S_{ij}	Strain-rate tensor (1/s)
u	Internal energy (J/kg)
q_i	Conductive heat flux (W/m^2)
k	Thermal conductivity (W/mK)
T	Temperature (K)
c_p	Heat capacity (J/K)
h	Heat transfer coefficient (W/m^{2}K)
A	Area (m^2)
Re	Reynolds number (-)
V	Velocity (m/s)
ν	Kinematic viscosity (m^2/s)
τ_w	Wall shear stress (Pa)

c_f	Skin friction coefficient (-)
u^*	Friction velocity (m/s)
u	Boundary layer velocity (m/s)
y	Wall distance (m)
δ	Boundary layer thickness (m)
g	Gravitational acceleration (m/s^2)
θ	Temperature (K)
k	Turbulent kinetic energy (m^2/s^2)
ε	Turbulent dissipation (m^2/s^3)
σ_θ	Turbulent Prandtl number (-)
ν_t	Turbulent viscosity (m^2/s)
ω	Specific dissipation (1/s)

Subscripts

i, j, k	Spacial dimension
w	Wall
∞	Bulk
t	Turbulent

Superscripts

$\overline{x}$	Mean
x'	Fluctuation
x^+	Non-dimensionality

Contents

List of Figures

List of Tables

1
Introduction

1.1 Background

In the fight against climate change there is a large effort to replace fossil fuel powered vehicles with electric ones. Electric cars and buses have become more common to see on the road and they are likely to become even more common in the future. To store the electrical energy required to power these vehicles large batteries are used which introduces new challenges for automotive manufacturers.
One of these challenges is thermal runaway (TR) where the overheating of a battery cell causes chemical degradation which releases stored energy as heat and gas. This overheats the surrounding cells and starts a chain reaction that can spread in the entire battery pack causing fire and in some cases explosions. This thesis will focus on simulating TR to gain a larger understanding of the computational methods and models used. This understanding can then be used to decrease the risk of TR and help in the development of safer electric vehicles.

1.2 Aim

The aim of this thesis is to perform CFD simulations of thermal runaway in a generic battery module containing 20 prismatic battery cells to predict propagation time between the battery cells. Additionally simulations implementing simple mitigation strategies such as cooling and improved insulation materials will be performed to investigate how the propagation time is affected.

1.3 Limitations

Like any project this thesis is subject to some limitations. Firstly, the geometries used are generic and simplified. Here all components are blocks of different dimensions and components like busbars are not included. Additionally, the internal chemistry and electronics of the battery cells are ignored. The battery cells are instead modelled to have similar thermal and mechanical properties as real battery cells. The thermal runaway behavior is also generic and not based on a specific real case.
The behaviour of the cells during TR is also generic. The gas released by each cell is set to be 100 grams with a composition of 97 % carbon dioxide and 3 % hydrogen gas by volume. This gas is then released during 4 seconds. In total each cell is limited

to release 3.5 MJ of energy as heat and the critical temperature of the battery cells to enter TR is set to be 383.15 K.
As this is a generic case there is no validation data available to directly compare with which limits the conclusions that can be drawn.

2
Theory

In this chapter the inner workings of lithium-ion batteries are explained in simple terms as well as the phenomenon of thermal runaway and the different conditions that cause it. Additionally computational fluid dynamics and its governing equations are discussed complete with a section on turbulence modelling.
The purpose of the theory is to support the method and results sections that follow.

2.1 Batteries

Batteries are devices that store chemicals that when allowed to react convert chemical energy to electrical energy. If the battery is rechargeable the process is reversed during charging and electrical energy is converted to chemical energy. Lithium-ion batteries (LIBs) do this by moving lithium ions back and forth during their operation, one way for charging and the other way for discharging, giving them the nickname "rocking chair batteries" [9].
A LIB is more than just the chemistry. All the reactions occur within what is called the battery cell. The cells are then connected in series and/or in parallel to form a battery module which also contains insulation between the cells, cooling and a casing to contain everything within. Battery modules can then be connected to form a battery pack. The application will determine the configuration of the battery pack and how many modules and cells it contains.
In electric vehicles battery cells appear in three main formats; cylindrical, prismatic and pouch cells. If an electric vehicle uses cylindrical cells it has thousands while if it uses pouch cells it only has hundreds and if it has prismatic cells it has dozens [5].

2.1.1 Parts of the LIB

To understand how LIBs work we must first be familiar with the different parts that make up the battery cell. The main parts are the two electrodes; anode and cathode, the separator and the electrolyte.
The anode and cathode are comprised of the active materials which are coated with metallic foils called current collectors, to increase electrical conductivity. The current collectors are connected through an external circuit. The active materials are what store and release the lithium ions and are different for the anode and cathode. In the anode carbon in the form of graphite is the most common active material while in the cathode the active material is a lithiated metal oxide or a lithiated metal phosphate such as lithium cobalt oxide (LCO) and lithium iron phosphate

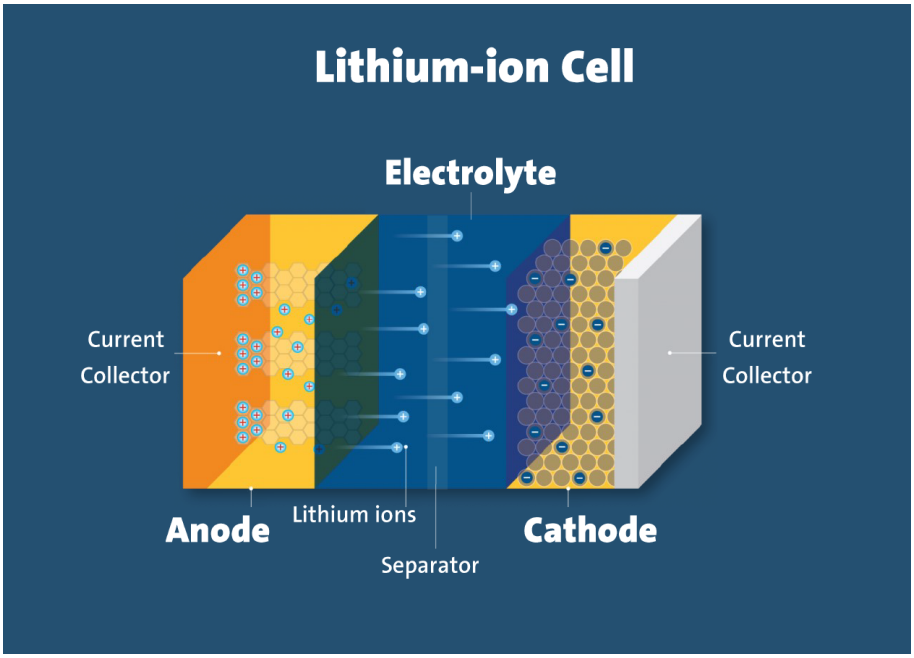

Figure 2.1: The parts of a lithium-ion battery [4].

(LFP), respectively. In chemistry anode and cathode refer to what reaction occurs at the electrodes. However, that is not important in the scope of this thesis so for simplicity and in the interest of avoiding confusion anode will refer to the carbon based electrode and cathode will refer to the metallic electrode. This definition is also used in literature.
To avoid the battery cell short circuiting by the anode and cathode touching a separator is placed between the terminals. The separator is electrically non conductive and porous to allow the passage of lithium ions in the electrolyte. It is most often made out of a polymer such as polyethylene or polypropylene.
The electrolyte is what enables the lithium ions to travel between the anode and cathode, without it the battery does not function. The most of the electrolyte is composed of an organic solvent in which a lithium salt such as lithium hexaflourophosphate ($LiPF_6$) is dissolved. There can also be additives in the electrolyte to change its properties, for instance to make it more flame retardant or to protect the cathode. The lithium ions are transported by solvent particles in the electrolyte and when the ions reach the anode or cathode the bond to the solvent particles is released and the ions move into the active material [9].
In figure 2.1 the different parts discussed above are shown.

2.1.2 How LIBs work

In a charged state the lithium atoms are stored in the anode surface. When discharging starts an oxidation reaction occurs on the anode and the lithium atoms releases one electron each and become ions. The ions are carried by the electrolyte solvent particles through the separator to the cathode surface where they are stored in a process called intercalation. The electrons flow through the current collector

and in the circuit connected to the cathode current collector. The flow of electrons induce a current which is used to power whatever electric device is connected to the circuit. The lithium ions react with the electrons in the cathode in a reduction reaction and become neutrally charged atoms again. When all the lithium has moved from the anode to the cathode the battery is fully discharged and there is no more current delivered.
During charging the opposite happens. Current is supplied in the circuit which caused the lithium atoms in the cathode to release electrons through an oxidation reaction and then travel as ions through the separator to the anode surface where they are stored through intercalation. A reduction reaction occurs on the anode as the ions have their electrons returned and they again become neutrally charged atoms. The charging is complete when all lithium has moved from the cathode to the anode [9].

2.1.3 Solid electrolyte interphase

The solid electrolyte interphase (SEI) is a thin protective layer that is formed where the anode active material meets the electrolyte. It is comprised of lithium salts and solvents from the electrolyte as well as lithium ions. The SEI layer is ionically conductive but slows down the flow of lithium ions. It is also electrically insulating. The protective layer is formed during the first operating cycle of charge and discharge of the battery cell. How fast this first cycle is will determine the thickness of the SEI layer and is therefore very important to battery manufacturers. A thicker layer will be more protective but also contain more ions, lowering the capacity of the battery. A thinner layer will have a larger capacity but will risk cracking. If a crack is formed lithium ions will be used to repair it which will lower the capacity of the battery [9].

2.2 Thermal runaway

As the temperature of a battery cell increases above its maximal operating temperature several exothermic reactions occur which unless stopped continue to increase the temperature. Ordered from low to high temperature they are: SEI layer decomposition, separator pores closing, electrolyte break down and gas formation, separator melting, cathode breakdown and oxygen generation and lastly lithium melting. At what temperatures these reactions occur depends on the cell chemistry. When the electrolyte breaks down several chemical reactions take place which generates several gases such as carbon dioxide, carbon monoxide, methane, ethane, ethylene and hydrogen. Unless vented through a safety vent these gases increase the pressure within the cell which puts great strain on the cell walls which may break if the pressure is too big. When the separator melts the electrodes are no longer separated and an internal short circuit (ISC) occurs. When the cathode breaks down oxygen is released which is what enables big fires. The battery cell has entered thermal runaway when the reaction is not able to be stopped. At what temperature TR occurs depends on the battery chemistry. Figure 2.2 shows approximate temperatures for the reactions in a generic battery cell.
Once one cell in the battery module has entered thermal runaway there is a risk that

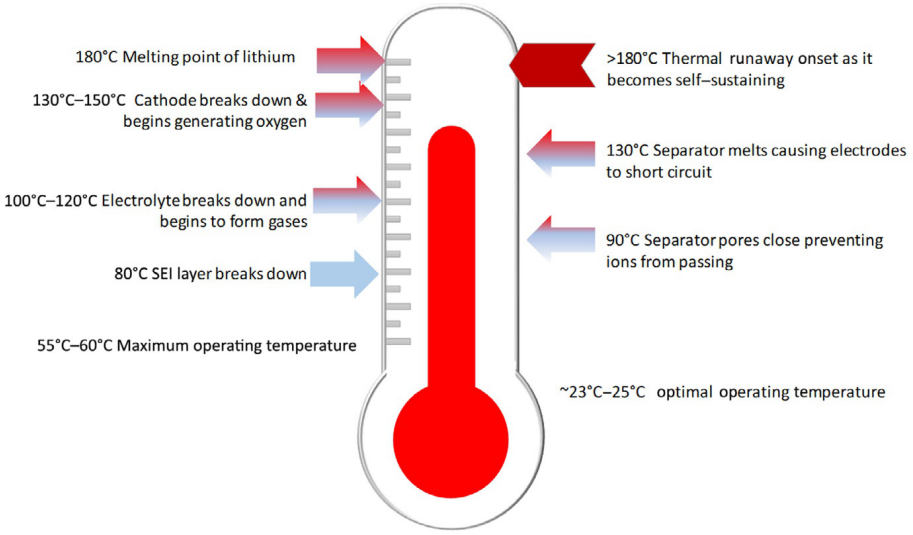

Figure 2.2: Approximate temperatures for the different exothermic reactions occurring in a battery cell [9]

it will propagate to the neighboring cells at which point the entire battery pack is at risk. The heat is transferred through conduction and convection. Limiting the effect of these transport modes is paramount for battery thermal safety [9]. Conduction is limited by using insulating materials and heat sinks while convection can be limited by ensuring good air flow to dispel the hot air and vented gases.
Thermal runway can happen spontaneously but often times there is some cause for it to be triggered. The main causes for TR are mechanical, electrical and thermal abuse. Common for these causes is that they lead to an internal short circuit and fast increase in temperature. ISC is the largest contributor to the heating of the battery cell out of all the exothermic reactions, generating 26.3% of the heat. Internal defects in the battery cell can cause spontaneous ISC that are independent of any abuse condition which can lead to TR. The state of the battery will impact the likelihood and severity of TR. A battery with higher state of charge will have more energy stored which can be converted to more heat in the event of an ISC [3]. Below the different abuse conditions are described.

2.2.1 Mechanical abuse

The battery can be subjected to mechanical abuse in many ways such as vibration, shock, impact, extrusion and penetration. The most dangerous forms of mechanical abuse are impact and penetration and both can occur in a car crash. Impact means that the battery is subjected to a large force on the outside. This force can crush the battery which damages the internals and causes an ISC and can lead to an explosion if the state of charge is large enough. Penetration means that a foreign object, typically metallic, makes its way into the battery, also causing an ISC. Both of these conditions open up the battery which can lead to the electrolyte, or if they have been generated, gases leaking out. During battery testing the nail penetration test is a common way to get trigger an ISC [3].

2.2.2 Electrical abuse

There are many forms of electrical abuse as well. High rate charge and discharge are one abuse case that lowers the trigger temperature for TR of a battery cell as well as decreasing the propagation time to neighboring cells. The reasons for the increased risk of TR is the heat generation during charging as well as high lithium concentration in the anode with high state of charge. An external short circuit can occur if the battery is deformed or in contact with water and can increase the temperature of the battery cell, however not enough to trigger TR. Overcharge is when the battery cell is charged above its intended capacity. This damages the battery cell and leads to heat generation until the it is so damaged that it breaks open and TR is triggered. Over-discharge also damages the battery cell but does not directly lead to heat generation and TR, rather the damage make the battery cell more susceptible to other abuse cases, and therefore TR, in the future [3].

2.2.3 Thermal abuse

The heat generated in the above described abuse conditions is classed as thermal abuse as well as other sources of overheating. One such source of overheating can be improper connections with battery connectors and the most obvious source of overheating is a hot environment. The increase in temperature as a result of the overheating starts the exothermic reactions described above which ultimately lead to TR [7].

2.3 CFD

The process of numerically solving fluid dynamics using computer code is known as computational fluid dynamics (CFD). It is a powerful simulation technique that is used in many different fields to predict a wide range of different physical phenomena. Compared to physical experiments CFD is cheap to perform and the the level of detail of results obtained can be refined as much as desired. It also offers greater flexibility as the parameters of the simulated system can easily be changed which enables many simulations to be run in an effective and systematic manner which, for example, allows the optimization of geometry through parametric studies.
When working with CFD the first step is pre-processing. Here the geometry of the problem is either imported from an external CAD software or created in the CFD tool. When created the geometry is called the computational domain. The domain is then spatially discretized into many smaller control volumes according to the finite volume method (FVM). The control volumes can have different size and shape depending in the problem. The spatial discretization results in a computational mesh where the control volume are called cells. It is in each cell that the computations are performed. Generating the mesh is a critical step when performing CFD as both the accuracy of the simulation as well as the computational time is dependent in the number of cells. To optimize the accuracy to cost ratio the mesh is most often refined in areas of interest where the variation in for example velocity or temperature is expected to be large while the mesh is allowed to be more coarse in areas where

these variations are expected to be smaller. When a grid has been generated the fluid properties and boundary conditions are defined.
The next is to solve the problem. This is done by discretizing the governing equations which are differential equations into algebraic expressions. The algebraic expressions share one or more variables which means they cannot be solved directly and must be solved iteratively. The simulation is complete when the solution has converged. Finally the results are post-processed and visualized in a way that conveys the desired information through for example contour or vector plots [8].

2.3.1 Governing equations

The three equations that govern fluid flow are the continuity equation (2.2), momentum equation (2.9) and energy equation (2.15). These equations are derived from three conservation laws of physics. These laws are: the conservation of mass, Newton's second law and the first law of thermodynamics [8]. The continuity equation and momentum equation are together called the Navier-Stokes equations.

Continuity equation

In a control volume mass is conserved which yields the continuity equation:

$$\frac{d\rho}{dt} + \rho\frac{\partial v_i}{\partial x_i} = 0 \tag{2.1}$$

where ρ is the fluid density, t is time, v_i is the velocity in the i-direction and x_i is the spacial coordinate in the i-direction.
If the flow velocity is below 1/3 the speed of sound the flow can be assumed to be incompressible which means that density is constant. The continuity equation then becomes [1]:

$$\frac{\partial v_i}{\partial x_i} = 0 \tag{2.2}$$

Momentum equation

Newton's second law states that the rate of change of momentum of an object, in this case a control volume, is equal to the sum of forces acting on it [8]. This results in the momentum equation which in its most basic form is given by:

$$\rho\frac{dv_i}{dt} = \frac{\partial \sigma_{ij}}{\partial x_i} + \rho f_i \tag{2.3}$$

where σ_{ji} is the stress tensor and f_i is the volume force vector.
The stress tensor, σ_{ij}, is given as:

$$\sigma_{ij} = -p\delta_{ij} + \tau_{ij} \tag{2.4}$$

where p is pressure which acts on the surface of the fluid element, δ_{ij} is the Kronecker delta which takes a value of 1 if $i = j$, else it is 0. Lastly τ_{ij} is the viscous stress tensor which is defined as:

$$\tau_{ij} = 2\mu S_{ij} - \frac{2}{3} S_{kk}\delta_{ij} \tag{2.5}$$

where μ is the fluid dynamic viscosity and S_{ij} is the strain-rate tensor.
The strain-rate tensor, S_{ij}, is expressed in terms of velocity gradients:

$$S_{ij} = \frac{1}{2}\left(\frac{\partial v_i}{\partial x_j} + \frac{\partial v_j}{\partial x_i}\right) \tag{2.6}$$

Combining equations 2.3, 2.4 and 2.5 we get:

$$\rho\frac{dv_i}{dt} = -\frac{\partial p}{\partial x_i} + \frac{\partial \tau_{ji}}{\partial x_j} + \rho f_i = -\frac{\partial p}{\partial x_i} + \frac{\partial}{\partial x_j}\left(2\mu S_{ij} - \frac{2}{3}\mu\frac{\partial v_k}{\partial x_k}\delta_{ij}\right) + \rho f_i \tag{2.7}$$

which is the momentum equation in its full form.
For incompressible flow and constant dynamic viscosity equation (2.7) can be reduced to [1]:

$$\rho\frac{dv_i}{dt} = -\frac{\partial p}{\partial x_i} + \mu\frac{\partial^2 v_i}{\partial x_j \partial x_j} + \rho f_i \tag{2.8}$$

Changing from $\frac{d}{dt}$ to $\frac{\partial}{\partial t}$ we get:

$$\rho\frac{\partial v_i}{\partial t} + \rho v_j\frac{\partial v_i}{\partial x_j} = -\frac{\partial p}{\partial x_i} + \mu\frac{\partial^2 v_i}{\partial x_j \partial x_j} + \rho f_i \tag{2.9}$$

which will be used later.

Energy equation

The first law of thermodynamics states that rate of change of internal energy in a control volume is equal to the rate of change of both heat addition (or subtraction) and work done on (or by) the volume [8]. The energy equation is defined as:

$$\rho\frac{du}{dt} = \sigma_{ji}\frac{\partial v_i}{\partial x_j} - \frac{\partial q_i}{\partial x_i} + \rho z \tag{2.10}$$

where u is internal energy of the fluid element, q_i is the conductive heat flux across the faces of the fluid element in the i-direction and z is the radiative heat source.
The heat flux, q_i is given by Fourier's law:

$$q_i = -k\frac{\partial T}{\partial x_i} \tag{2.11}$$

where k is the thermal conductivity and T is the temperature.
By using equations (2.4) and (2.11) in equation (2.10) we obtain the full energy equation for compressible flow:

$$\rho\frac{du}{dt} = -P\frac{\partial v_i}{\partial x_i} + \frac{\partial}{\partial x_i}\left(k\frac{\partial T}{\partial x_i}\right) + \rho z + \Phi \tag{2.12}$$

where Φ is a dissipation term that is given by:

$$\Phi = 2\mu \left(S_{ij} - \frac{1}{3} S_{kk} \delta_{ij} \right)^2 > 0 \tag{2.13}$$

and represents irreversible viscous heating.
For incompressible flow we have:

$$du = c_p dT \tag{2.14}$$

where c_p is the heat capacity of the fluid which is assumed to be constant. With the continuity equation (2.2) equation and neglecting radiation (2.12) becomes [1]:

$$\rho c_p \frac{dT}{dt} = \Phi + \frac{\partial}{\partial x_i} \left(k \frac{\partial T}{\partial x_i} \right) \tag{2.15}$$

2.3.2 Heat transfer

The transfer of energy that occurs due to differences in temperature is called heat. Heat transfer is used to predict how much and how fast energy is transferred within and between bodies. Heat has three modes of being transferred: conduction, convection and radiation. [2]

Conduction

The heat transfer within a body or between bodies that are in contact (including solid-fluid contact) is called conduction and is described by Fourier's law (2.11). The reason for the right hand side being negative is because heat transfers from high to low temperature [2].

Convection

Convection is heat transfer that is connected to the movement of fluid.
The heat flux from convection is given by Newton's law of cooling:

$$q = hA(T_w - T_\infty) \tag{2.16}$$

where h is the heat transfer coefficient, A is the contact area, T_w is wall temperature of the solid body and T_∞ is the temperature of the fluid. The heat transfer coefficient, h, can be estimated analytically for some cases or is determined through experiment. Values of h for common situations can be found in tables in literature.
Due to the no-slip condition of the fluid there is no convection at the interface, instead heat is transported through conduction. The effect of convection becomes stronger and more dominant further from the wall where the velocity is larger.
There exist two types of convection: natural and forced. Natural convection is when the warm body causes movement of the fluid. The body heats the closest fluid which changes its density creating a density gradient. The density gradient induces motion due to gravity and buoyancy and thus a velocity gradient is also created. Forced convection is the opposite, movement of the fluid causes heat to be transported from the body. In practice these types of convection often happen simultaneously, resulting in mixed convection [2].

Radiation

The energy transferred through radiation is caused by electromagnetic radiation and thus it does not require a medium to travel through. A so called blackbody is the ideal thermal radiator and emits energy according to the Stefan-Boltzmann law of thermal radiation:

$$q = \sigma A T^4 \tag{2.17}$$

where σ is the Stefan-Boltzmann constant ($\sigma = 5.669 \cdot 10^{-8} W/m^2 \cdot K^4$). In a more realistic case more parameters have to be accounted for. A body that emits radiation also receives some. Real bodies are seldom ideal blackbodies, instead they have an emissivity, ϵ, that is less than 1. All radiation emitted by one body is also not all received by the other body because electromagnetic radiation requires line of sight to be transmitted between bodies. With these parameters considered equation (2.17) becomes:

$$q = F_\epsilon F_G \sigma A \left(T_1^4 - T_2^4\right) \tag{2.18}$$

where F_ϵ is the emissivity function, F_G is the view factor function that accounts for line of sight and T_1 and T_2 is the temperature of two bodies [2].

2.3.3 Capturing the boundary layer

The boundary layer is the region closest to the wall and is formed as a result of the no-slip condition and viscosity of the fluid. This creates a velocity gradient from the wall to the bulk-flow. Capturing this region during discretization is important to obtain an accurate result from the simulation as the boundary layer affects drag and heat transfer. The boundary layer is defined to span from the wall to the distance normal to the wall that has a velocity equal to 99% of the free stream velocity. Depending on the flow different equations are used to describe the boundary layer. In this thesis the equations for flat plates will be described as it is the most similar to the flow in the battery module.

Parameters

In boundary layer flows there are many important parameters. First is the Reynolds number which is often said to be the most important non-dimensional number in fluid mechanics. It relates the inertial to viscous forces in a flow and is used to determine if the flow is laminar or turbulent. It is defined as:

$$Re_L = \frac{\rho V L}{\mu} = \frac{V L}{\nu} \tag{2.19}$$

where V is the fluid velocity, L is the characteristic length and ν is the kinematic viscosity. For a flat plate turbulent flow is regarded to begin when $Re_L \sim 5 \cdot 10^5$, below this number flow is assumed to be laminar.
Next is the wall shear stress, τ_w, which is the shear stress that the fluid exerts on the wall. It is defined by:

$$\tau_w = \frac{c_f \rho V^2}{2} \tag{2.20}$$

where c_f is the skin friction coefficient that can be approximated in different ways or obtained empirically. An approximation for laminar flow is:

$$c_f = \frac{0.664}{\sqrt{Re_L}} \tag{2.21}$$

and for turbulent flow:

$$c_f = \frac{0.027}{{Re_L}^{1/7}} \tag{2.22}$$

The final parameter is the friction velocity, u^*, which is given by [10]:

$$u^* = \sqrt{\frac{\tau_w}{\rho}} \tag{2.23}$$

Sub-layers

The boundary layer can be divided into three different sub-layers: the wall layer, the overlap layer and the outer layer. The wall layer is closest to the wall and in this layer viscous shear dominates the flow, in the outer layer turbulent shear dominates and in the overlap layer both types of shear are important.
In the overlap layer the boundary layer velocity, u, is defined as:

$$\frac{u}{u^*} = \frac{1}{\kappa} \ln \frac{y u^*}{\nu} + B \tag{2.24}$$

where κ and B are dimensionless constants equal to 0.41 and 5.0, respectively. This is called the logarithmic law, or log-law for short.
In the wall layer a different relation called the wall law holds:

$$u^+ = \frac{u}{u^*} = \frac{y u^*}{\nu} = y^+ \tag{2.25}$$

where the superscript "+" denotes non-dimensionality, i.e. u^+ and y^+ are non dimensional velocity and position from the wall, respectively. y^+ is used to determine which law is to used. For values of $y^+ < 5$ the wall law is used and for $y^+ > 30$ the log-law is used. In the region where $5 < y^+ < 30$ there are no exact correlations [10].

Thickness

The thickness of the boundary layer, δ depends on if the flow is laminar or turbulent and on the Reynolds number. For laminar flow it is:

$$\delta = \frac{5L}{\sqrt{Re_L}} \tag{2.26}$$

and for turbulent flow:

$$\delta = \frac{0.16L}{Re_L^{1/7}} \tag{2.27}$$

We see that for turbulent flow the boundary layer is thicker [10].

2.3.4 Turbulence and its modelling

Turbulence is a complex phenomena that is present in almost all flow that we encounter. For this reason methods to compute it must be used in CFD. Turbulent flow has a number of characteristics that define it. First, as mentioned in 2.3.3, turbulent flow occurs at high Reynolds numbers. At what Reynolds number depends on the flow, for example it is lower for pipes than for flat plates. Turbulence is also multi-scale, containing eddies that range in size from the flow length scale to tiny eddies that require a very high resolution grid to resolve, yet these smallest length scales are much larger than the molecular scale so the continuum assumption holds. The smallest eddies dissipate their kinetic energy into thermal energy due to viscous forces and are destroyed as their energy is depleted. The small eddies get their energy from slightly larger eddies which get their energy from even larger eddies and so on in what is called the cascade process. Turbulence increases diffusivity and the exchange of momentum in the flow which delays flow separation and increases wall friction and heat transfer [1].

Turbulence models

There are many different ways to model turbulence. In this thesis RANS models, and more specifically eddy-viscosity models, will be considered. These are among the most simple turbulence models and are therefore not as computationally expensive such as more sophisticated models such as Large Eddy Simulations (LES) or Detached Eddy Simulations (DES). If turbulence is not modelled and instead resolved Direct Numerical Simulations (DNS) are used. This is the most accurate method but also the most computationally expensive [1].

Reynolds Averaged Navier-Stokes

In turbulent flow the variables are decomposed into a mean and a fluctuating part. For the velocity it looks like:

$$v_i = \bar{v_i} + v_i' \tag{2.28}$$

The bar represents the mean part that is time averaged as:

$$\bar{v} = \frac{1}{2T}\int_{-T}^{T} v dt \tag{2.29}$$

where T is a sufficiently large time step.
By applying the decomposition in equation (2.28) to the Navier-Stokes equations (2.2) and (2.9) the Time-averaged Navier-Stokes equations or Reynolds Averaged Navier-Stokes (RANS) equations are obtained:

$$\frac{\partial \bar{v_i}}{\partial x_i} = 0 \tag{2.30}$$

$$\rho \bar{v_j} \frac{\partial \bar{v_i}}{\partial x_j} = \rho \bar{f_i} - \frac{\partial \bar{p}}{\partial x_i} + \frac{\partial}{\partial x_j} \left(\mu \frac{\partial \bar{v_i}}{\partial x_j} - \rho \overline{v_i' v_j'} \right) \tag{2.31}$$

Time averaging removes the time-term which means that the mean flow is assumed to be steady. The final term on the right hand side of equation (2.31), $\rho \overline{v_i' v_j'}$, is the Reynolds stress tensor. In total there are ten unknowns that need to be found in order to solve the RANS equations: the velocity (3), the pressure (1) and the Reynolds stresses (6). This is called the closure problem and it is solved by introducing turbulence models.
The most accurate turbulence model is to derive exact equations for the Reynolds stresses from the Navier-Stokes equations. This yields the Reynolds stress equation:

$$\begin{aligned} \frac{\partial \overline{v_i' v_j'}}{\partial t} + \underbrace{\bar{v_k} \frac{\partial \overline{v_i' v_j'}}{\partial x_k}}_{C_{ij}} = & \underbrace{-\overline{v_i' v_k'} \frac{\partial \bar{v_j}}{\partial x_k} - \overline{v_j' v_k'} \frac{\partial \bar{v_i}}{\partial x_k}}_{P_{ij}} + \underbrace{\overline{\frac{p'}{\rho} \left(\frac{\partial v_i'}{\partial x_j} + \frac{\partial v_j'}{\partial x_i} \right)}}_{\Pi_{ij}} \\ & \underbrace{-\frac{\partial}{\partial x_k} \left[\overline{v_i' v_j' v_k'} + \frac{\overline{p' v_j'}}{\rho} \delta_{ik} + \frac{\overline{p' v_i'}}{\rho} \delta_{jk} \right]}_{D_{ij,t}} + \underbrace{\nu \frac{\partial^2 \overline{v_i' v_j'}}{\partial x_k \partial x_k}}_{D_{ij,\nu}} \\ & \underbrace{-g_i \beta \overline{v_j' \theta'} - g_j \beta \overline{v_i' \theta'}}_{G_{ij}} \underbrace{-2\nu \overline{\frac{\partial v_i'}{\partial x_k} \frac{\partial v_j'}{\partial x_k}}}_{\varepsilon_{ij}} \end{aligned} \tag{2.32}$$

where θ is temperature, β is volumetric thermal expansion and g_i is gravitational acceleration.
The equation can be simplified and expressed symbolically as:

$$C_{ij} = P_{ij} + \Pi_{ij} + D_{ij} + G_{ij} - \varepsilon_{ij} \tag{2.33}$$

where C_{ij} is the convection term, P_{ij} production, Π_{ij} pressure-strain, D_{ij} total diffusion (which is the sum of turbulent $D_{ij,t}$ and viscous diffusion $D_{ij,\nu}$), G_{ij} buoyancy production and ε_{ij} dissipation [1].

The Boussinesq assumption

The Reynolds stresses can be modelled by a turbulent viscosity, ν_t, according to the Boussinesq assumption. The diffusion term in the RANS equation (2.31) after dividing by density then becomes:

$$\frac{\partial}{\partial x_j} \left[\nu \left(\frac{\partial \bar{v_i}}{\partial x_j} + \frac{\partial \bar{v_j}}{\partial x_i} \right) - \overline{v_i' v_j'} \right] = \frac{\partial}{\partial x_j} \left[(\nu + \nu_t) \left(\frac{\partial \bar{v_i}}{\partial x_j} + \frac{\partial \bar{v_j}}{\partial x_i} \right) \right] \tag{2.34}$$

An expression for the Reynolds stress tensor can be obtained from equation (2.34):

$$-\overline{v_i'v_j'} = \nu_t \left(\frac{\partial \bar{v}_i}{\partial x_j} + \frac{\partial \bar{v}_j}{\partial x_i} \right) \tag{2.35}$$

Equation (2.35) is not valid when $i = j$ due to the continuity equation (2.30) setting the right hand side equal to 0. This is remedied by adding the trace of the left hand side to the right hand side:

$$\overline{v_i'v_j'} = -\nu_t \left(\frac{\partial \bar{v}_i}{\partial x_j} + \frac{\partial \bar{v}_j}{\partial x_i} \right) + \frac{1}{3}\delta_{ij}\overline{v_k'v_k'} = -2\nu_t \bar{S}_{ij} + \frac{2}{3}\delta_{ij}k \tag{2.36}$$

The turbulent viscosity is not a physical parameter like regular viscosity, rather it is dependent on the mean flow gradients and turbulence and can therefor vary throughout the domain [1].

Kinetic energy

Turbulent kinetic energy, k, is an important variable in the RANS models. It is defined as the sum of the normal Reynolds stresses:

$$k = \frac{1}{2}\left(\overline{v_1'^2} + \overline{v_2'^2} + \overline{v_3'^2}\right) \equiv \frac{1}{2}\overline{v_i'v_i'} \tag{2.37}$$

The exact equation for turbulent kinetic energy is obtained by taking the trace of the Reynolds stress equation (2.32) and dividing by two:

$$\begin{aligned} \frac{\partial k}{\partial t} + \underbrace{\bar{v}_j \frac{\partial k}{\partial x_j}}_{C^k} = & \underbrace{-\overline{v_i'v_j'}\frac{\partial \bar{v}_i}{\partial x_j}}_{P^k} \underbrace{-\nu \overline{\frac{\partial v_i'}{\partial x_j}\frac{\partial v_i'}{\partial x_j}}}_{\varepsilon} \\ & \underbrace{-\frac{\partial}{\partial x_j}\left[v_j' \left(\frac{p'}{\rho} + \frac{1}{2} v_i'v_i' \right) \right]}_{D_t^k} + \underbrace{\nu \frac{\partial^2 k}{\partial x_j \partial x_j}}_{D_\nu^k} \underbrace{-g_i \beta \overline{v_i'\theta'}}_{G^k} \end{aligned} \tag{2.38}$$

In the same way as for the Reynolds stress equation the k-equation can be expressed symbolically:

$$C^k = P^k + D^k + G^k - \varepsilon \tag{2.39}$$

where the symbols have the same meaning as for equation (2.33) [1].

Dissipation

The equation for turbulent dissipation, ε, is based on the k-equation and has the symbolic formulation:

$$C^\varepsilon = P^\varepsilon + D^\varepsilon + G^\varepsilon - \Psi^\varepsilon \tag{2.40}$$

where Ψ^ε is a destruction term. P^k and ε from the k-equation are used to describe the production, buoyancy and destruction terms. To get the correct units they are multiplied by $\frac{\varepsilon}{k}$ and unknown coefficients are added:

$$P^{\varepsilon} + G^{\varepsilon} - \Psi^{\varepsilon} = \frac{\varepsilon}{k}(c_{\varepsilon 1}P^k + c_{\varepsilon 1}G^k - c_{\varepsilon 2}\varepsilon) \tag{2.41}$$

which finally gives the full equation for dissipation:

$$\frac{\partial \varepsilon}{\partial t} + \bar{v_j}\frac{\partial \varepsilon}{\partial x_j} = \frac{\varepsilon}{k}(c_{\varepsilon 1}P^k + c_{\varepsilon 1}G^k - c_{\varepsilon 2}\varepsilon) + D^{\varepsilon} \tag{2.42}$$

Because the production, destruction and turbulent diffusion terms are modelled the ε-equation is also modelled [1].

The $k - \varepsilon$ model

In the k-equation (2.39) and ε-equation (2.42) the production term, P^k, buoyancy term, G^k and turbulent diffusion term, D^k and D^{ε}, are unknown and need to be modelled. By modelling these terms the full modelled equations for k and ε are obtained which form the $k - \varepsilon$ model.
First, the production term is modelled according to the Boussinesq assumption (2.36):

$$P^k = \underbrace{\left[\nu_t\left(\frac{\partial \bar{v_i}}{\partial x_j} + \frac{\partial \bar{v_i}}{\partial x_j}\right) - \frac{2}{3}\delta_{ij}k\right]}_{\text{Boussinesq assumption}}\frac{\partial \bar{v_i}}{\partial x_j} = 2\nu_t \bar{S_{ij}}\bar{S_{ij}} \tag{2.43}$$

Then, the buoyancy term is modelled. It is given in equation (2.38) as:

$$G^k = -g_i\beta\overline{v_i'\theta'} \tag{2.44}$$

The term $\overline{v_i'\theta'}$ is handled by the Boussinsq assumption:

$$\overline{v_i'\theta'} = -\alpha_t\frac{\partial \bar{\theta}}{\partial x_i} \tag{2.45}$$

where α_t is turbulent thermal diffusivity and is given by:

$$\alpha_t = \frac{\nu_t}{\sigma_\theta} \tag{2.46}$$

where σ_θ is the turbulent Prandtl number, an empirical constant set to $0.7 < \sigma_\theta < 0.9$, which relates how well the turbulence transports momentum to how well it transports thermal energy, similar to the regular Prandtl number. The buoyancy term thus becomes:

$$G^k = g_i\beta\frac{\nu_t}{\sigma_\theta}\frac{\partial \bar{\theta}}{\partial x_i} \tag{2.47}$$

Lastly, the turbulent diffusion term is given by:

$$\begin{aligned} D^k &= \frac{\partial}{\partial x_j}\left[\left(\nu + \frac{\nu_t}{\sigma_k}\right)\frac{\partial k}{\partial x_j}\right] \\ D^{\varepsilon} &= \frac{\partial}{\partial x_j}\left[\left(\nu + \frac{\nu_t}{\sigma_\varepsilon}\right)\frac{\partial \varepsilon}{\partial x_j}\right] \end{aligned} \tag{2.48}$$

for k and ε, respectively.
Inserting the modelled terms (2.43), (2.47) and (2.48) into the k-equation (2.38) and the ε-equation (2.42) results in the full modelled equations for k and ε:

$$\frac{\partial k}{\partial t} + \bar{v_j}\frac{\partial k}{\partial x_j} = \nu_t \left(\frac{\partial \bar{v_i}}{\partial x_j} + \frac{\partial \bar{v_j}}{\partial x_i}\right)\frac{\partial \bar{v_i}}{\partial x_j} + g_i \beta \frac{\nu_t}{\sigma_\theta}\frac{\partial \bar{\theta}}{\partial x_i} - \varepsilon + \frac{\partial}{\partial x_j}\left[\left(\nu + \frac{\nu_t}{\sigma_k}\right)\frac{\partial k}{\partial x_j}\right] \tag{2.49}$$

$$\frac{\partial \varepsilon}{\partial t} + \bar{v_j}\frac{\partial \varepsilon}{\partial x_j} = \frac{\varepsilon}{k} c_{\varepsilon 1}\nu_t \left(\frac{\partial \bar{v_i}}{\partial x_j} + \frac{\partial \bar{v_j}}{\partial x_i}\right)\frac{\partial \bar{v_i}}{\partial x_j} + c_{\varepsilon 1} g_i \frac{\varepsilon}{k}\frac{\nu_t}{\sigma_\theta}\frac{\partial \bar{\theta}}{\partial x_i} - c_{\varepsilon 2}\frac{\varepsilon^2}{k} + \frac{\partial}{\partial x_j}\left[\left(\nu + \frac{\nu_t}{\sigma_\varepsilon}\right)\frac{\partial \varepsilon}{\partial x_j}\right] \tag{2.50}$$

where the turbulent viscosity is given by:

$$\nu_t = c_\mu \frac{k^2}{\varepsilon} \tag{2.51}$$

The values for the constants are presented in table 2.1 [1].

The $k - \omega$ SST model

On its own the $k - \varepsilon$ model has two major drawbacks, it has trouble dealing with adverse pressure gradients as well as reverse flow and it requires damping functions near walls. The $k - \omega$ model does not have these issues but it does have some issues of its own, mainly it depends on the free stream value of the specific dissipation, ω. In simple terms the $k - \varepsilon$ model is good in the free stream but bad near the walls while the $k - \omega$ model is bad in the free stream but good near the walls. The two models can be combined in $k - \omega$ Shear Stress Transport (SST) model where each model is used where it is best. The relation of ω to k and ε is given by:

$$\omega = \frac{\varepsilon}{\beta^* k} \tag{2.52}$$

where $\beta^* = c_\mu$. From this the equations for the $k - \varepsilon$ model can be transformed into those needed for the $k - \omega$ model. After some derivation which is omitted here the equations for the standard $k - \omega$ SST model are obtained as:

$$\frac{\partial k}{\partial t} + \frac{\partial}{\partial x_j}(\bar{v_j} k) = \frac{\partial}{\partial x_j}\left[\left(\nu + \frac{\nu_t}{\sigma_k}\frac{\partial k}{\partial x_j}\right)\right] + P^k - \beta^* k\omega \tag{2.53}$$

$$\begin{aligned}\frac{\partial \omega}{\partial t} + \frac{\partial}{\partial x_j}(\bar{v_j}\omega) = \frac{\partial}{\partial x_j}\left[\left(\nu + \frac{\nu_t}{\sigma_\omega}\frac{\partial \omega}{\partial x_j}\right)\right] + P^\omega - \beta\omega^2 \\ + 2(1 - F_1)\sigma_{\omega 2}\frac{1}{\omega}\frac{\partial k}{\partial x_i}\frac{\partial \omega}{\partial x_i}\end{aligned} \tag{2.54}$$

where P^ω is the production term for specific dissipation and is given as:

$$P^\omega = \alpha \frac{P^k}{\nu_t} \tag{2.55}$$

Table 2.1: Constants for $k-\varepsilon$ and $k-\omega$ SST turbulence models.

$k-\varepsilon$		$k-\omega$ SST			
c_μ	0.09	β^*	0.09	a_1	0.3
$c_{\varepsilon 1}$	1.44	$\alpha_{k-\omega}$	5/9	$\sigma_{k,k-\omega}$	0.85
$c_{\varepsilon 2}$	1.92	$\alpha_{k-\varepsilon}$	0.44	$\sigma_{k,k-\varepsilon}$	1
σ_k	1	$\beta_{k-\omega}$	3/40	$\sigma_{\omega,k-\omega}$	0.5
σ_ε	1.3	$\beta_{k-\varepsilon}$	0.0828	$\sigma_{\omega,k-\varepsilon}$	0.856

F_1 is a blending function that takes a value between 0 and 1 to smoothly switch from $k-\varepsilon$ mode to $k-\omega$ mode, and vice versa, depending on distance to the nearest wall, d. Near the wall in $k-\omega$ mode it takes a value of 1 and for $k-\varepsilon$ mode it takes a value of 0. The blending function is also used to blend the values of the coefficients. In the case if α it looks like:

$$\alpha = F_1\alpha_{k-\omega} + (1-F_1)\alpha_{k-\varepsilon} \tag{2.56}$$

The value of the blending function, F_1, is determined by:

$$F_1 = \tanh(\xi^4), \quad \xi = \min\left[\max\left(\frac{\sqrt{k}}{\beta^*\omega d}, \frac{500\nu}{d^2\omega}\right), \frac{4\sigma_{\omega_{k-\varepsilon}}k}{CD_\omega d^2}\right] \tag{2.57}$$

where CD_ω is:

$$CD_\omega = \max\left(2\sigma_{\omega_{k-\varepsilon}}\frac{1}{\omega}\frac{\partial k}{\partial x_i}\frac{\partial \omega}{\partial x_i}, 10^{-10}\right) \tag{2.58}$$

The turbulent viscosity, ν_t is determined differently than in the $k-\varepsilon$ model. Here it is given by:

$$\nu_t = \frac{a_1 k}{\max(a_1\omega, |\hat{s}|F_2)} \tag{2.59}$$

where $|\hat{s}|$ is given by:

$$|\hat{s}|^2 = \left(\frac{\partial \bar{v}_i}{\partial x_j} + \frac{\partial \bar{v}_j}{\partial x_i}\right)\frac{\partial \bar{v}_i}{\partial x_j} = 2\hat{s}_{ij}\hat{s}_{ij} \tag{2.60}$$

and F_2 is another blending function which is given by:

$$F_2 = tanh(\eta^2), \quad \eta = \max\left(\frac{2\sqrt{k}}{\beta^*\omega d}, \frac{500\nu}{d^2\omega}\right) \tag{2.61}$$

The coefficients used in the $k-\omega$ SST model are presented in table 2.1 [1].

3

Methods

In this chapter the methods used in this thesis are described. This includes a description and discussion of the used geometry, implemented models, meshing strategy as well as variations of the simulations.

3.1 Geometry

The geometry is created in the 3D-CAD tool in Star-CCM+. It consists of two rows of 10 battery cells which are blocks with dimensions 50 x 150 x 150 mm. Centered on the top of each battery cell is a circular vent with a 20 mm diameter. The cell is enclosed by an aluminum shell with thickness 0.5 mm which is modelled as a shell and not created as part of the geometry. Between the cells polyurethane foam plates are placed with a thickness of 2 mm and the same height and width as the cells. Between the rows of cells there is a gap of which is 20 mm wide. The cells and foam plates are placed on an aluminum cooling plate which is 8 mm thick and has a width such that there is an 10 mm gap to the side of the battery cells. Surrounding these parts is an aluminum case which is 2 mm thick. The height of the case is such that there is a 12 mm of empty space above the cells. On one of the short side faces of the case there is a 4 x 200 mm opening that is centered on the empty space above the cells that allows the vented gases to escape.

A geometry part for the gas domain is also created from a block that spans 100 mm out from the sides, top and back of the case and 200 mm from the front. The solid parts are then subtracted from the block which creates the domain for gas.

The geometry is shown in figures 3.1, 3.2 and 3.3. Darker blue is the polyurethane foam, lighter blue is the are the cell vents, grey is the battery cells, lighter grey is the cooling plate and darker grey is the case. Figure 3.4 shows the extent of the gas domain around the battery module.

In order to be able to refer to each battery cell individually they are labeled 1-20 with the first row containing cells 1-12 and the second row containing cells 11-20 as shown in figure 3.5.

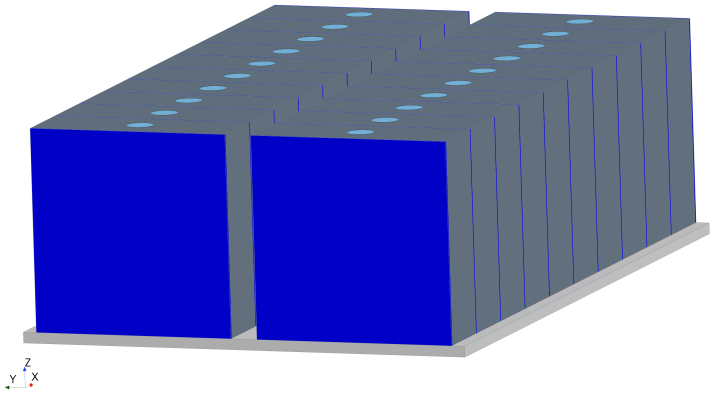

Figure 3.1: ISO view of the battery module without the case.

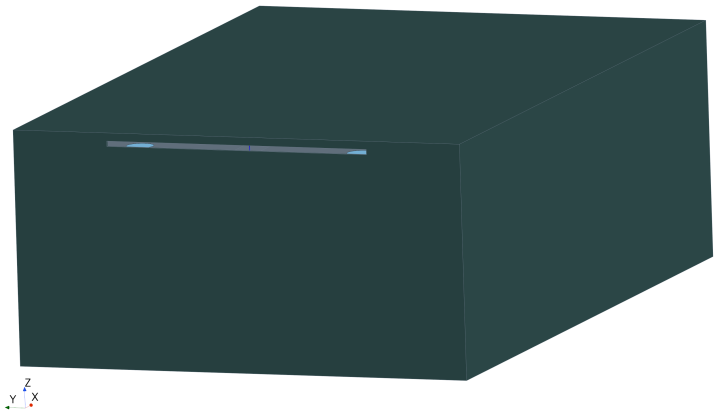

Figure 3.2: ISO view of the battery module with the case.

Figure 3.3: Front view of the module cross section.

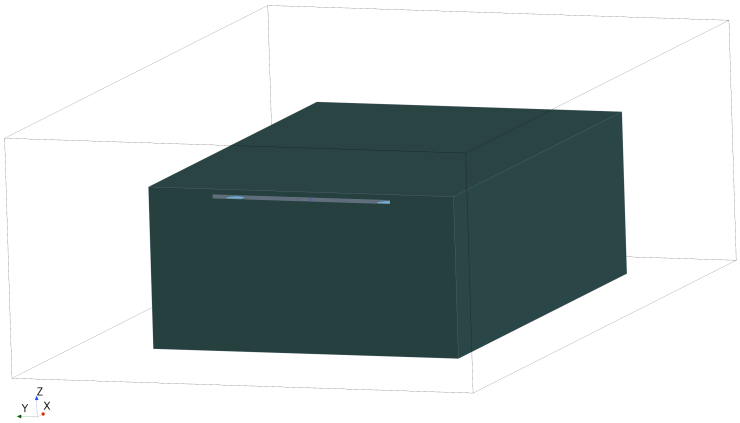

Figure 3.4: ISO view of the battery module with lines showing the extent of the gas domain.

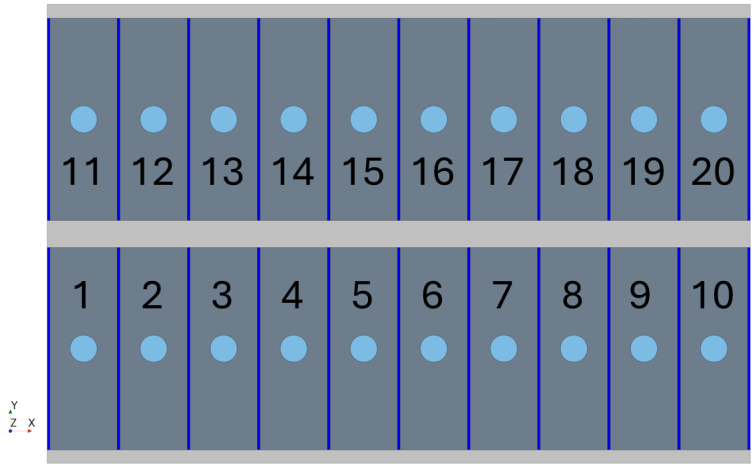

Figure 3.5: Top view of the battery module without the case. Battery cell numbering shown.

3.2 Boundaries and interfaces

The domain was divided into four regions: gas, battery cells, non battery cell solids and battery cell shells. Each region has its own set of boundaries defined by the geometry that are used to set boundary conditions and create interfaces between the regions which enables heat transfer.
All boundaries of the solid regions are set as wall. The outsides of the gas domain are set as pressure outlet with a specified gas mass fraction of 100% air. The boundaries of the gas domain in contact with the cells venting surfaces were set to be mass flow inlets. The mass flow, total temperature and gas compositions are defined by a table which is supplied to the solver and is shown in 3.1. The temperature is defined by its total, or stagnation, value because it is independent of velocity which will change

depending on the mass flow. The appropriate value for each of the parameters is set for each time step by reading the table and interpolating. After the four seconds of venting have passed the mass flow is again set to zero and the total temperature of the vent inlet is set to be the volume average temperature of the battery cell.
Interfaces that connect different regions are created using contact information obtained through an imprint operation. The interface between the shell region and the battery cells was created automatically upon the creation of the shell region. The other interfaces with the shell region were defined manually by selecting a boundary of the shell region and connecting it with the corresponding boundary of the region that was to be connected. The interfaces between non-shell regions were created by selecting both and creating boundary-mode interfaces and then selecting the surfaces the interface should apply to which in all cases except for the vents were all available contacts. Due to the non-conformal nature of the mesh with non matching faces all interfaces were set as mapped.
In order to trigger TR in the battery module the interface between the bottom of the first cell and the shell was set as a heat source of 10 kW before the onset of TR in that cell, after which it behaves as a normal interface with no heat source.

Table 3.1: Vent rate

			Species mass flow (%)		
Time	Mass flow (g/s)	Total temperature (K)	Air	CO2	H2
1	10.309652	700	0	95.64	4.36
1.5	18.557373	900	0	95.64	4.36
2	24.743164	1100	0	95.64	4.36
2.5	29.897989	1100	0	95.64	4.36
3	32.990885	1500	0	95.64	4.36
3.5	29.897989	1500	0	95.64	4.36
4	24.743164	1300	0	95.64	4.36
4.5	18.557373	1300	0	95.64	4.36
5	10.309652	1100	0	95.64	4.36
5.001	0	900	1	0	0

3.2.1 Initial conditions

In order to save time the battery cells and its shells were given an initial temperature of 373.15 K, 10 K below the critical temperature for TR. The other solids were initialized to 363.15 K and the gas was set to be still with a temperature of 300 K and consisting of 100% air.

3.3 Models

Each region had its own physics continua with a set of models created. Many models were shared between all regions and the solid regions shared many models as well.

Due to the unsteady nature of thermal runaway the model implicit unsteady was selected as the time model. The time step used is discussed in section 3.3.1.

A segregated solver was chosen for the flow and energy equations. In such a solver the governing equations are solved in an iterative manner to obtain the unknown variables such as the velocity components, pressure and temperature. This is in contrast to a coupled solver where all variables are solved for at the same time, requiring large equation systems. A segregated solver is best suited for incompressible flows but it can also handle compressible flows as long as the mach-number is relatively low. In general a segregated solver is faster and is preferably used in cases where it is applicable.

The turbulence was chosen to be modeled using the $k-\omega$ SST model because it combines the $k-\varepsilon$ and $k-\omega$ models such that they both are used where they are at their best. Because the value of y^+ was made to be less than one on all surfaces during the meshing a low y^+ wall treatment was selected. To see how the solution would differ with a different turbulence model the base mesh from the mesh refinement was used with the $k-\varepsilon$ model. The result from this is presented in section 4.2. All the selected models are presented in table 3.2.

The properties of the different materials used are presented in table 3.3. All materials except for battery cell and polyurethane are the default one supplied in Star-CCM+. The properties for the battery cell material were chosen to represent a generic battery cell. LIBs are anisotropic with their heat conductivity because they are built up of several different materials as described in section 2.1. To capture this the thermal conductivity was set to be much lower in the thin direction of the battery cells. The properties of the polyurethane were gathered from [6] which is a website with material data.

Table 3.2: Models used.

Shared models		
Three Dimensional	Cell quality Remeditation	Gradients
Implicit Unsteady	Solution interpolation	
Gas models		
Multi-Component Gas	Non-reacting	Ideal Gas
Segregated Flow	Segregated Fluid Temperature	Segregated Species
Turbulent	Reynolds-Averaged Navier-Stokes	K-Omega Turbulence
SST (Menter) K-Omega	Wall Distance	Low y+ Wall Treatment
Gravity		
Battery cell models		
Solid	Constant Density	Segregated Solid Energy
Battery	Circuit Model	
Battery cell shell models		
Solid	Constant density	Segregated Solid energy
Non battery cell solids models		
Multi-Component Solid	Multi-Part Solid	Constant density
Segregated Solid Energy		

Table 3.3: Material properties.

Solids			
	Battery cell	Polyurethane	Aluminum
Density (kg/m^3)	1500	417	2702
Specific heat (J/kg·K)	1000	1200	903
Thermal conductivity (W/m·K)	x: 1, y: 75, z: 75	0.0605	237
Gases			
	Air	CO2	H2
Molecular weight (kg/kmol)	28.9664	44.01	2.01594
Specific heat (J/kg·K)	1003.62	850.566	14292.3
Dynamic viscosity (Pa·s)	1.85508E-5	1.49396E-5	8.87789E-6

3.3.1 Time step

Due to the vastly varying time scales of the simulation a dynamic time step is defined. This saves computational time by using a larger time step when not much is happening and then using a smaller time step when it is needed to capture the physics. The dynamic time step automatically decreases when thermal runaway is about to be triggered and then it decreases further when TR is triggered. After a while the time step starts to increase again, in steps, up to the largest value. An example of how the dynamic time step can vary in time is shown in figure 3.6 where the red dotted lines are TR events. The exact definition of the time step is shown below:

```
Time step = 0.25 s
if Volume average temperature of any cell > 380 K and no TR:
    Time step = 0.05 s
else if 380 < Volume average temperature of any cell < 382.65:
    Time step = 0.025 s
else if Volume average temperature of any cell > 382.65 K:
    Time step = 0.01 s
    if TR triggered:
        if Time passed since last TR < 5 s:
            Time step = 0.01 s
        else if Time passed since last TR < 6 s:
            Time step = 0.25 s
        else if Time passed since last TR < 7 s:
            Time step = 0.5 s
        else if Time passed since last TR < 8 s:
            Time step = 0.1 s
        else if Time passed since last TR < 9 s:
            Time step = 0.15 s
        else if Time passed since last TR < 10 s:
            Time step = 0.2 s
        else:
            Time step = 0.25 s
```

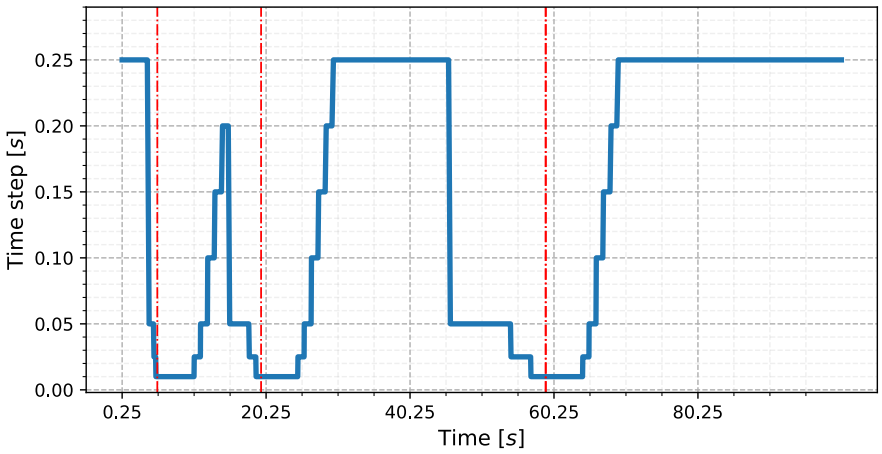

Figure 3.6: Example of how the dynamic time step changes over time.

3.3.2 Thermal runaway model

The thermal runaway model for batteries is relatively new in Star-CCM+ as it was introduced in 2023. It works by supplying data from an ARC-test which contains heat rates depending on temperature. This defines how fast and hot the TR process will be in the simulation. Another input to this model is the total amount of released energy. Finally a critical temperature is given to the model from which it knows when to trigger TR.

After the thermal runaway has been defined the battery cell parts are selected to be battery objects and the set-up is complete.

The ARC-data used in this thesis was taken from the tutorial supplied by Simcenter accessed through the Star-CCM+ user manual. It is shown in table 3.4.

Table 3.4: Heat rate table.

Temperature (K)	Heat rate (W)
283.15	300
311.15	600
350.15	3000
384.15	12000
411.15	40471.182
436.15	102694.7664
455.15	142044.9264
476.15	169296.7896
530	157296.7896
560	133845.6
580	112061.28
618.15	76669.2
650.15	38970.72
688.15	15337.56
774.15	5580
875.15	3720
994.15	1116.186

3.4 Meshing

Generating a high quality mesh is an integral part of a CFD analysis. Below the setting used to generate the mesh in Star-CCM+ as well as the outline for a mesh independence study are presented.

3.4.1 Global settings

The different geometry parts were meshed in different mesh operations all using polygonal cells. The first battery cell and the two contacting foam were meshed first and then a volume pattern was used to copy the mesh to the other cells and foam which decreased the meshing time. In the next operation the rest of the solids, the cooling plate and case, were meshed and in the final operation the gas region was meshed. Using different mesh operations results in a non-conformal mesh, meaning that faces of contacting parts meshed in different operation do not match one-to-one. To reduce the amount of interpolation between faces needed to resolve across interfaces the target surface sizes at these locations were made to be the same size in both mesh operations involved. Further, to obtain a good transition from prism layer cells to bulk mesh the target surface sizes were kept small. In the gas domain refinement was added in areas where high gradients were expected such as in the opening of the case and above the vents of the cells. Using a base size of 10 mm the relative size of all surface and volume refinements were obtained. The resulting generated mesh is from here on referred to as the baseline mesh.

3.4.2 Prism layers

To ensure a value of $y^+ < 1$ on all surfaces the prism layer mesher was used with the wall thickness definition mode where the number of prism layers, first cell height and total prism layer thickness are input parameters. By using the equations in section 2.3.3 an expression for y^+ is obtained:

$$y^+ = \frac{y_P \rho}{\mu} \sqrt{\frac{c_f V^2}{2}} \tag{3.1}$$

Here y_P is the cell center. To obtain the first cell height y_P is doubled and the following expression is obtained:

$$y_{firstcell} = 2y_P = 2\frac{y^+ \mu}{\rho V} \sqrt{\frac{2}{c_f}} \tag{3.2}$$

The total thickness of the prism layers is a geometric series that can be expressed as:

$$y_{total} = y_{firstcell} \left(\frac{1 - r^N}{1 - r} \right) \tag{3.3}$$

where r is the growth rate and N is the number of layers. Equations (3.2) and (3.3) are inserted into a spreadsheet and the growth rate and number of layers are adjusted such that the prism layer thickness is greater than the boundary layer thickness according to equation (2.26) or (2.27) depending on the Reynolds number. A value for the Reynolds number is obtained by estimating the maximum velocity that will occur during the simulation. What is known is the mass flow, total temperature and properties of the gas as well as the area the gas will pass through. The mass flow can be expressed as:

$$\dot{m} = V \rho A \tag{3.4}$$

where A is the area of the battery cell vent. The density can be substituted using the ideal gas law:

$$p = \rho R T \tag{3.5}$$

where R is the gas constant for the gas being vented. The temperature of the gas being vented is given as the total temperature of the gas, therefore we need to convert it to static conditions using:

$$T = T_o - \frac{V^2}{2c_P} \tag{3.6}$$

where T_o is the total temperature. The expression for the velocity then becomes:

$$V = -\frac{c_P \left(pA - \sqrt{\frac{c_P p^2 A^2 + 2\dot{m}^2 T R^2}{c_P}} \right)}{\dot{m} R} \tag{3.7}$$

With the properties of the gases in table 3.3 and the vent rate in table 3.1 an guess for the velocity is obtained which is used to predict the Reynolds number.

This results in an initial guess for the prism layers. The simulation is then run and the values of y^+ on all surfaces are observed. If the resulting value of y^+ is above one in a specific area the first cell height in that area is divided by the observed value of y^+ and is used in the next attempt.
Three distinct areas in the geometry were identified that needed their separate prism layer settings to obtain the desired y^+ due to different flow conditions. These areas were: all surfaces inside of the case, the surfaces outside of the case and the surface of the case opening. The final prism layer settings obtained after several iterations for the different areas are shown in table 3.5.

Table 3.5: Prism layer settings.

	Inside case	Outside case	Opening
First cell height (mm)	1.86E-3	1.62E-2	1.44E-3
Number of layers	13	12	15
Total thickness (mm)	0.513	0.839	2.26

3.4.3 Thin mesh

The thin mesher was used in the solid parts. This mesher generates uniform prismatic cells of high quality in areas that the mesher deems as thin which reduces the number of cells generated without compromising accuracy. In solid parts that have conduction in mainly one direction thin cells are appropriate to use. The threshold for generating thin cells was set to 2 mm which made the foam and case deemed thin and thus the thin cells were generated in these parts.

3.4.4 Mesh independence

The creation of the mesh is a trade-off between accuracy and computational time. In order to optimize this trade-off mesh independence studies are conducted for most, if not all, CFD-projects. The goal of a mesh independence study is to find, and use, the coarsest mesh possible that still obtains accurate results. This is done by creating a number of meshes with varying degree of fineness and then comparing the results obtained from them after running the simulation. Ideally the results will converge after which point the solution is independent of the mesh. At what point the results are considered mesh independent is up to the engineer performing the simulation and can depend on many different factors. In this thesis a variation of less than 1% between meshes was chosen to be the criteria for a mesh independent result.
To save time the geometry was reduced to only contain four battery cells, in a two by two configuration. This reduces the total cell count as well as reducing the total simulated time required to observe TR in all cells, both of which reduces the computational time. It was assumed that an independent mesh for the reduced geometry would be independent for the full geometry as well.
Using the baseline mesh described above with the relative sizes of the refinement the base size was simply changed to obtain one coarser and one finer mesh. The

coarser mesh had a base size of 20 mm and the finer mesh had a base size of 5 mm. The generated meshes were compared by multiple metrics: time of TR trigger for the four cells and the heat transfer from the shell of cell 2 to the contacting surfaces. The results from the mesh independence study are shown in section 4.1.

3.5 Variations

To simulate different cases than the one described above small alterations were made to the setup.

3.5.1 Effect of turbulence model

To assess the impact of the selected $k-\omega$ SST turbulence model the baseline mesh was run with the $k-\varepsilon$ model as well. In Star-CCM+ the model "Realizable K-Epsilon Two-Layer" was chosen with "Two-Layer All y+ Wall Treatment" as it is flexible and applicable in many situations. The same metrics of comparison were gathered as for the mesh independence study. Additionally the flow field was visualized using two different methods to asses the impact of the turbulence model on flow movement and recirculation. The first method was a LIC representation of the velocity vector field and the second method was to use streamlines emitted from the venting surface on the first cell. The results are presented in section 4.2. The same independence criteria of 1% as in the mesh independence study was used to compare the turbulence models.

3.5.2 Effect of cooling

As per the aim of this thesis cooling was also implemented. A custom field function was created that made the cooling plate into a negative heat source after the onset of TR in the first cell. A cooling power of 3 kW was implemented as it was deemed realistic with current methods.

3.5.3 Reduced foam thermal conductivity

By reducing the thermal conductivity of the polyurethane the effect of using better thermal insulation between the battery cells can be studied. For simplicity, the thermal conductivity was halved and the new value used was 0.03025 W/m·K.

4

Results

In this chapter the results obtained by using the methods described in the previous chapter are presented. First are the results from the mesh independence study and comparison of different turbulence models. After that follow the results from the three different cases: no cooling, cooling and reduced foam thermal conductivity. Finally graphs comparing the three cases are presented.

4.1 Mesh independence study

The results from the mesh independence study described in section 3.4.4 are presented in table 4.1. By subtracting the time of TR for cell 1 from the time of TR for the other cells and then dividing by the values for the fine mesh and subtracting one the variation from the fine mesh in % is obtained and is shown in figure 4.1. Similarly the variation for heat transfer is shown in figure 4.2.

Table 4.1: Result of mesh independence study.

	Coarse	Baseline	Fine
Number of cells	1 469 042	5 715 584	20 429 724
Time of TR cell 1 (s)	5.145	5.135	5.250
Time of TR cell 2 (s)	19.960	19.555	19.550
Time of TR cell 3 (s)	60.135	59.120	59.690
Time of TR cell 4 (s)	60.135	59.080	59.240
HT to gas (W)	-2 439.453	-2 687.533	-2 822.350
HT to cooling plate (W)	5 977.045	6 002.903	6 018.417
HT to foam (W)	520.247	521.941	522.555

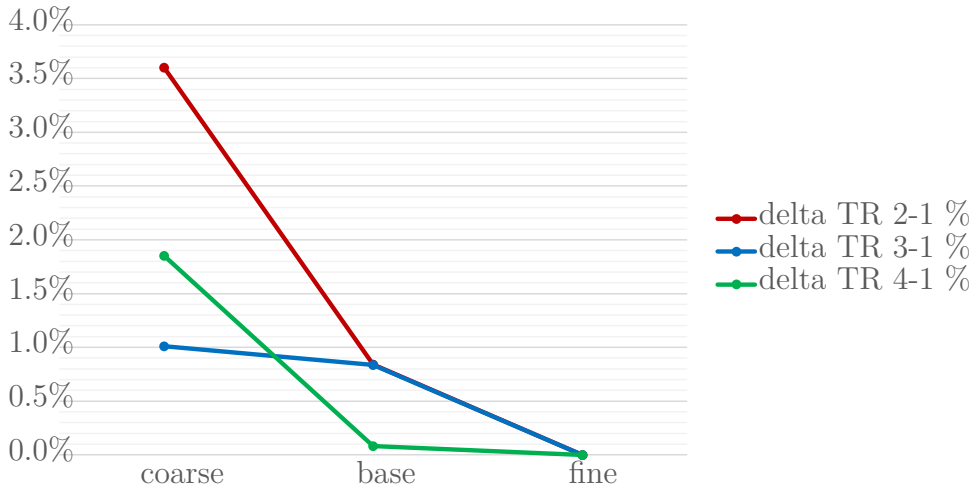

Figure 4.1: Convergence of time of TR trigger with respect to mesh fineness.

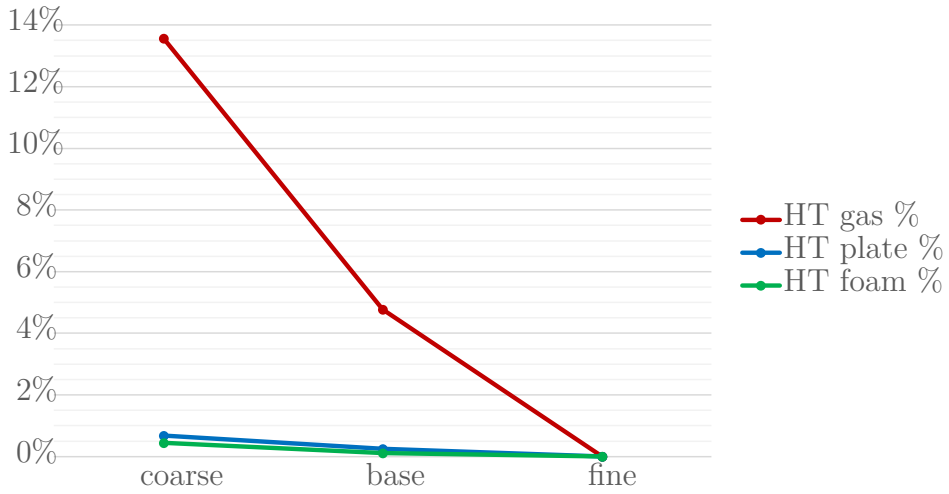

Figure 4.2: Convergence of heat transfer to contacting parts with respect to mesh fineness.

4.2 Effect of turbulence model

The different results obtained using different turbulence models for the baseline mesh are presented in table 4.2 along with a column showing the difference in results as a percentage. The velocity vector field at t=5.175 s is shown in figures 4.3 and 4.4 for the $k-\omega$ SST and $k-\varepsilon$ models respectively. Figures 4.5 and 4.6 show the streamlines emitted from the venting surface of the first cell at $t = 5.745$ s for the $k-\omega$ SST and $k-\varepsilon$ models respectively.

Table 4.2: Effect of turbulence model.

	$k-\omega$ SST	$k-\varepsilon$	% difference
Time of TR cell 1 (s)	5.135	5.135	0
Time of TR cell 2 (s)	19.555	19.630	0.384
Time of TR cell 3 (s)	59.120	61.110	3.366
Time of TR cell 4 (s)	59.080	61.910	4.790
HT to gas (W)	-2 687.533	-2 425.800	9.739
HT to cooling plate (W)	6 002.903	6011.180	0.138
HT to foam (W)	521.941	522.429	0.093

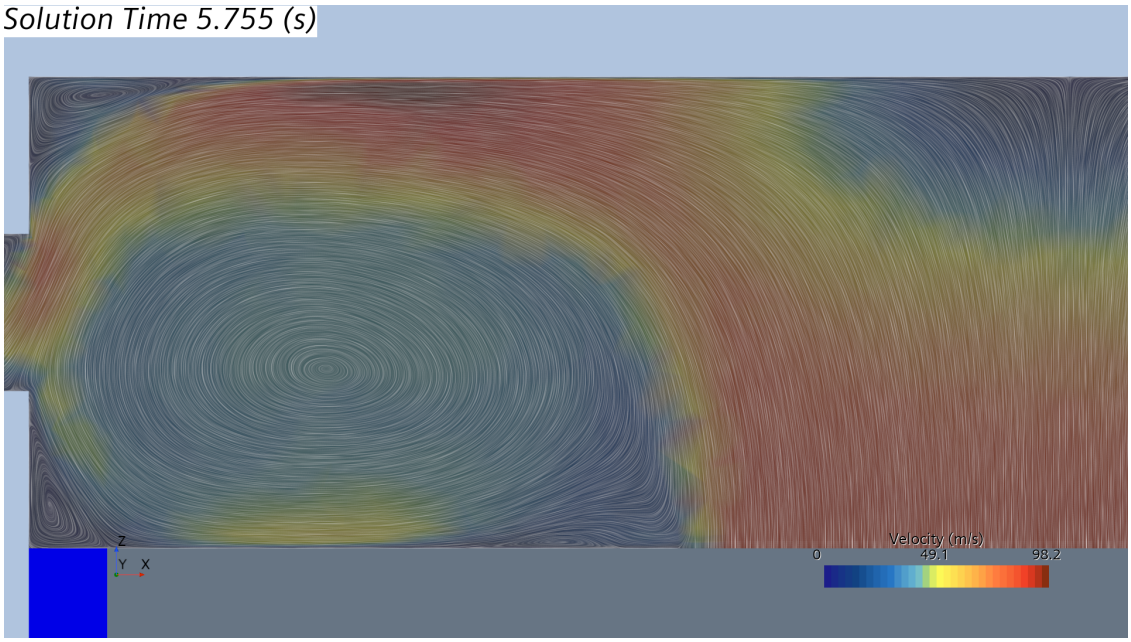

Figure 4.3: Velocity vector field using $k - \omega$ SST model at t=5.745 s.

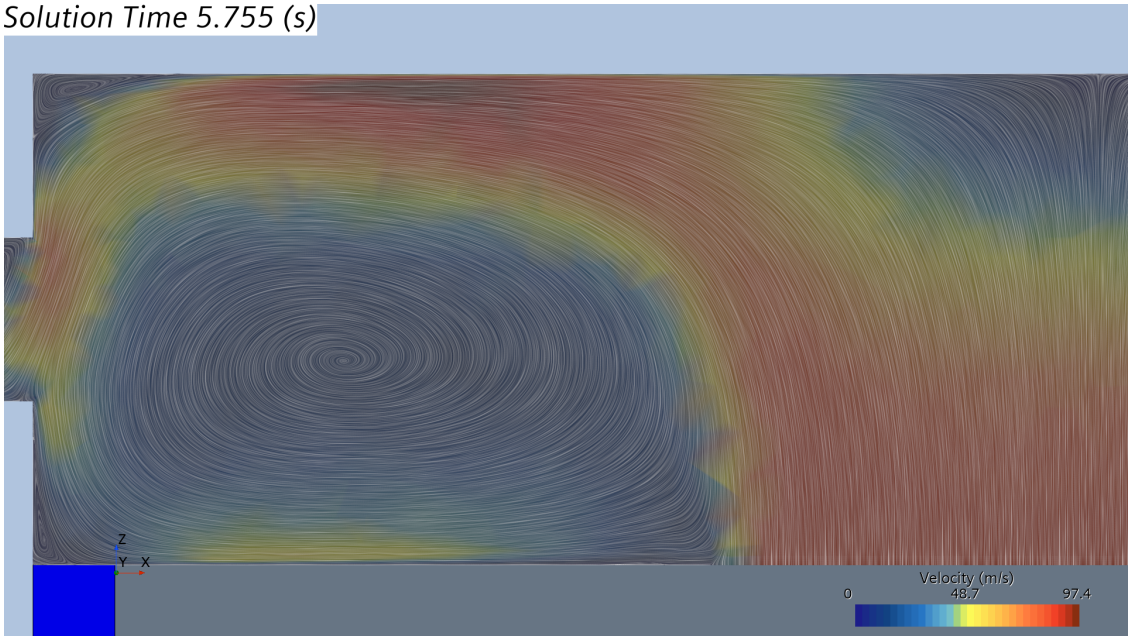

Figure 4.4: Velocity vector field using $k - \varepsilon$ model t=5.745 s.

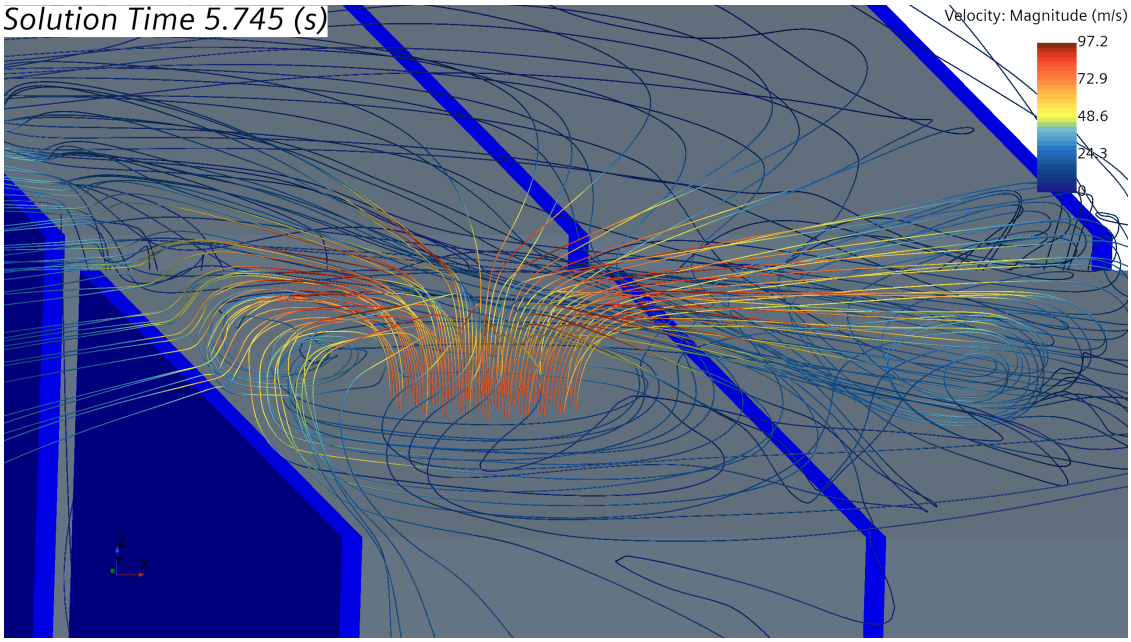

Figure 4.5: Streamlines using $k-\omega$ SST model at t=5.745 s.

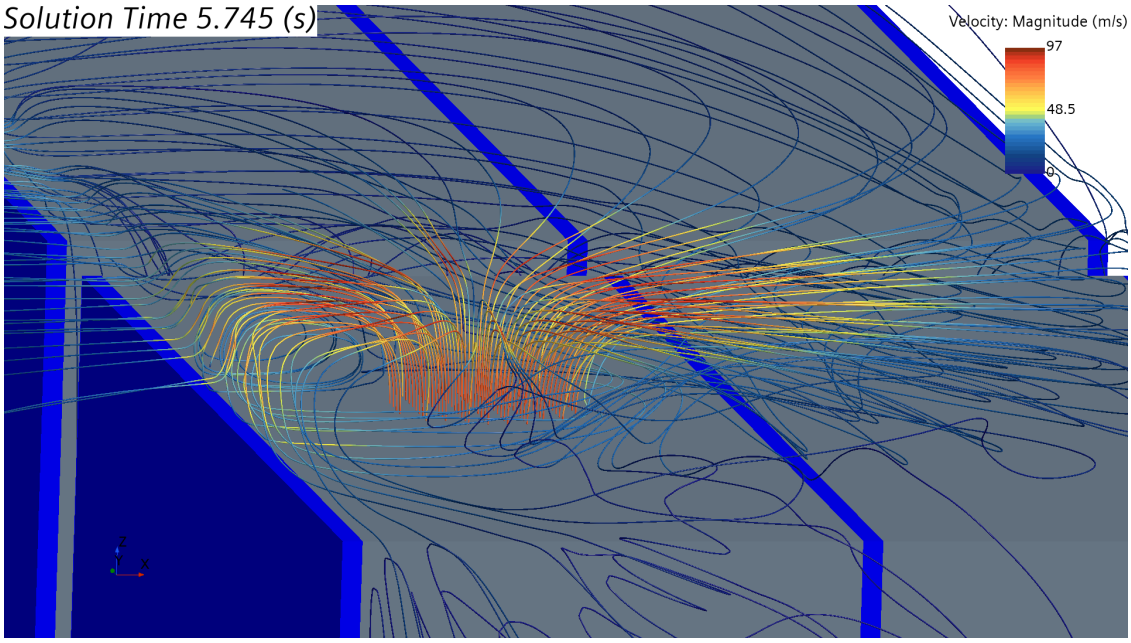

Figure 4.6: Streamlines using $k-\varepsilon$ model at t=5.745 s.

4.3 No cooling

The times of thermal runaway with no cooling are presented in table 4.3. Figure 4.7 shows the volume average temperature of each battery cell as a functions of time and figures 4.8, 4.9 and 4.10 show the mass flow from each vent as well as the total temperature of the vent inlet and the resulting velocity also as functions of time. The heat transfer out of cells 2, 12 and 20 are shown in figures 4.11, 4.12 and 4.13 respectively. The heat transfer is broken down into which other part the battery cell is in contract with. A positive value means that the heat is transferred from the battery cell to its surrounding and a negative value means that heat is transferred from the surroundings to the battery cell. Similar figures for battery cells 4, 6, 8, 10, 14, 16 and 18 as well as the maximum temperature of the battery cells as a function of time are presented in appendix A.1.

Table 4.3: Time of thermal runaway with no cooling for each battery cell.

Cell number	Time of TR (s)	Cell number	Time of TR (s)
Cell 1	5.135	Cell 11	63.035
Cell 2	19.45	Cell 12	65.64
Cell 3	33.635	Cell 13	68.62
Cell 4	46.135	Cell 14	72.5
Cell 5	57.655	Cell 15	76.86
Cell 6	67.015	Cell 16	81.035
Cell 7	74.93	Cell 17	85.135
Cell 8	81.94	Cell 18	89.425
Cell 9	87.55	Cell 19	92.66
Cell 10	92.2	Cell 20	96.55

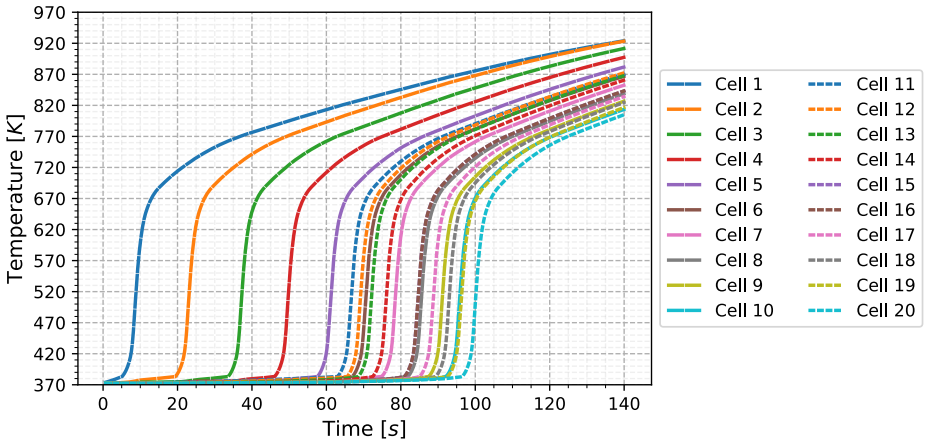

Figure 4.7: Volume average temperature of battery cells with no cooling implemented.

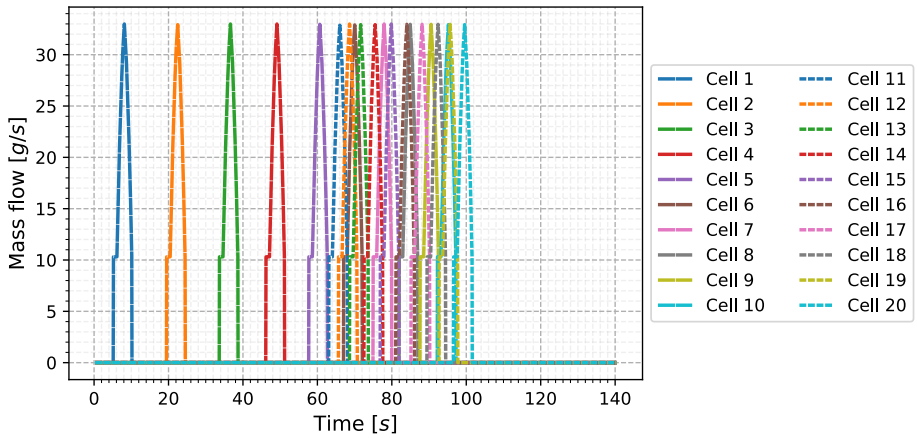

Figure 4.8: Mass flow from venting surfaces.

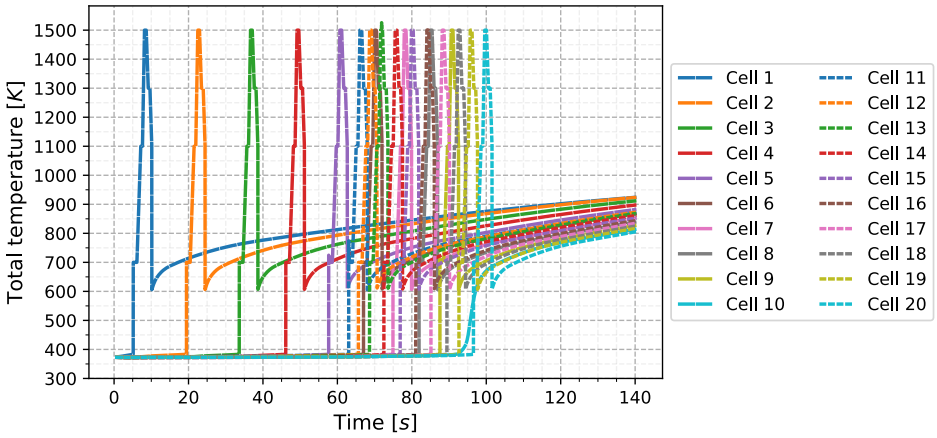

Figure 4.9: Vent inlet total temperature.

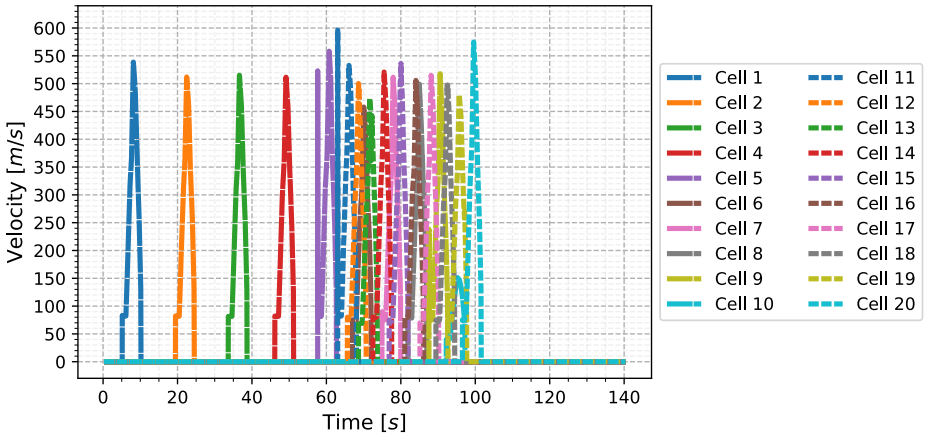

Figure 4.10: Velocity of vented gasses.

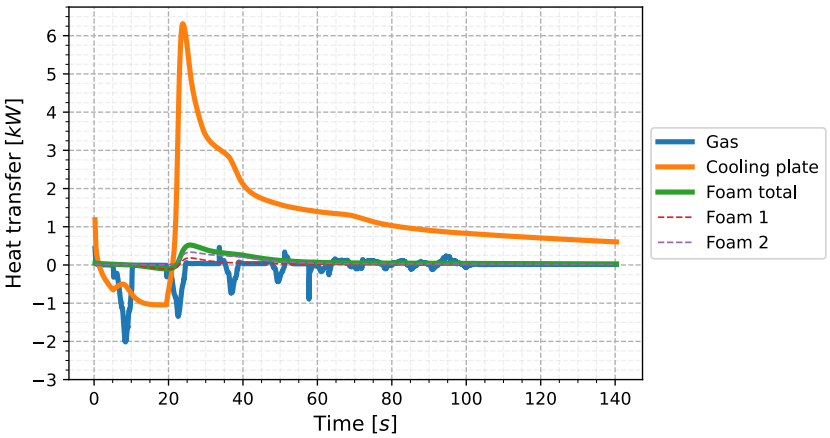

Figure 4.11: Heat transfer out of cell 2 with no cooling implemented.

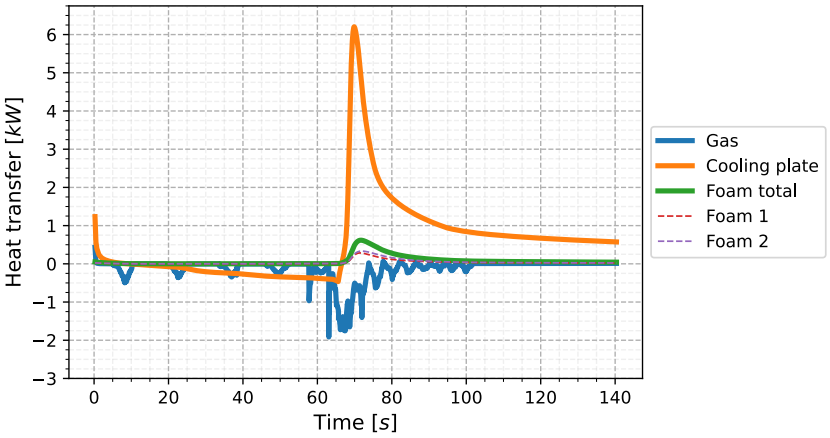

Figure 4.12: Heat transfer out of cell 12 with no cooling implemented.

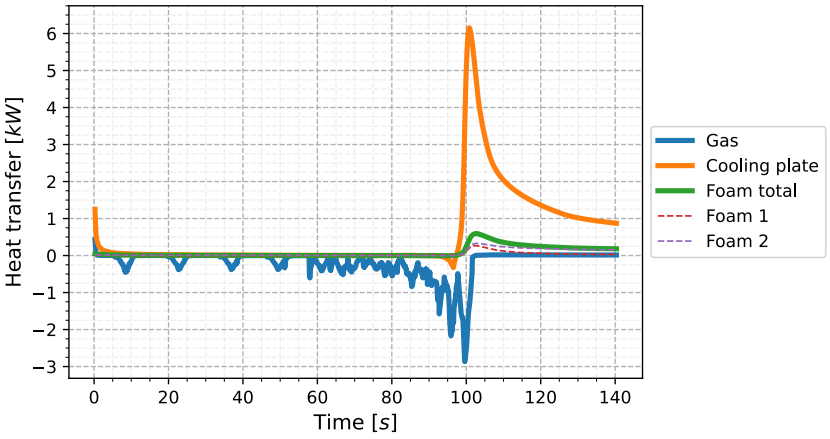

Figure 4.13: Heat transfer out of cell 20 with no cooling implemented.

4.4 Cooling

The results from implementing cooling are presented in a similar way to the results of no cooling. The times of thermal runaway with cooling are presented in table 4.4. Figures 4.14, 4.15, 4.16 and 4.17 show the volume average temperature and heat transfer out of cells 2, 12 and 20 respectively. In appendix A.2 the remaining figures for the heat transfer as well as the maximum cell temperature as a function of time can be found.

Table 4.4: Time of thermal runaway with cooling for each battery cell.

Cell number	Time of TR (s)	Cell number	Time of TR (s)
Cell 1	5.135	Cell 11	69.4
Cell 2	19.86	Cell 12	72.32
Cell 3	34.865	Cell 13	75.64
Cell 4	48.57	Cell 14	80.04
Cell 5	61.78	Cell 15	85.68
Cell 6	73.695	Cell 16	91.375
Cell 7	84.16	Cell 17	97.46
Cell 8	93.945	Cell 18	103.785
Cell 9	102.055	Cell 19	108.4
Cell 10	109.01	Cell 20	114.07

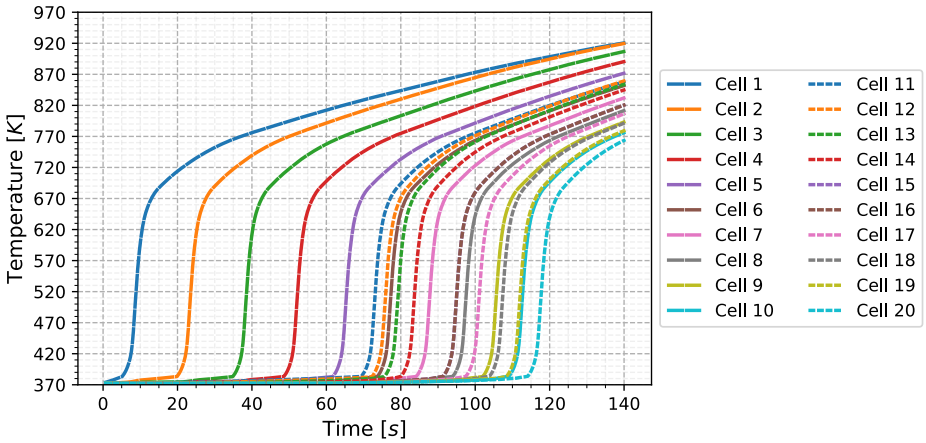

Figure 4.14: Volume average temperature of battery cells with cooling implemented.

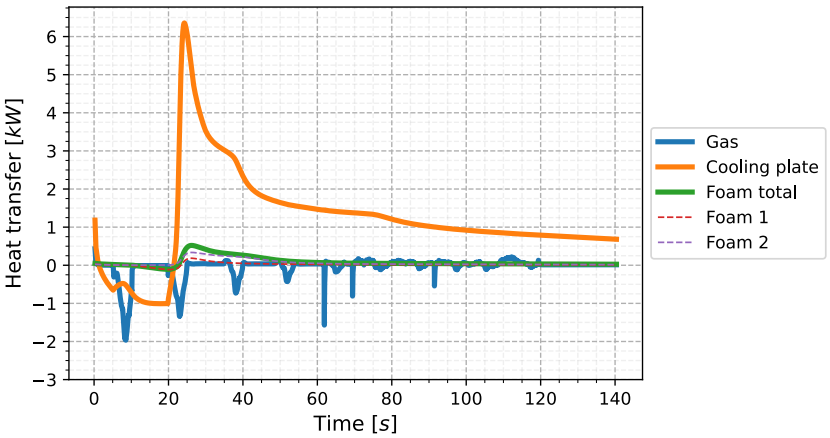

Figure 4.15: Heat transfer out of cell 2 with cooling implemented.

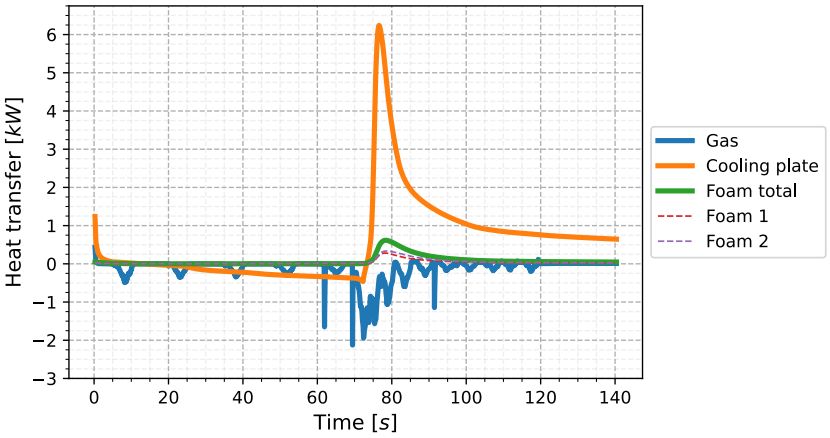

Figure 4.16: Heat transfer out of cell 12 with cooling implemented.

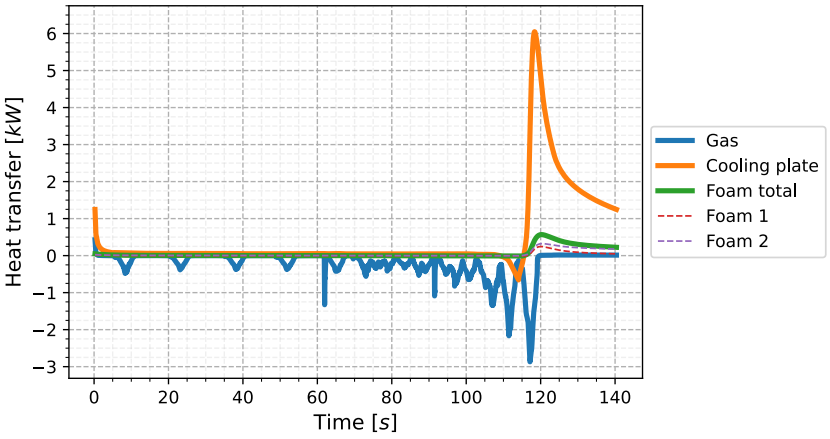

Figure 4.17: Heat transfer out of cell 20 with cooling implemented.

4.5 Reduced foam thermal conductivity

With a reduction of the foams thermal conductivity the times of thermal runaway obtained are presented in table 4.5. The volume average temperature of the cells and heat transfer out of cells 2, 12 and 20 are shown in figures 4.18, 4.19, 4.20 and 4.21 respectively. The remaining figures for heat transfer out of the cells can be found in appendix A.3.

Table 4.5: Time of thermal runaway with more insulating foam between each battery cell.

Cell number	Time of TR (s)	Cell number	Time of TR (s)
Cell 1	5.125	Cell 11	64.23
Cell 2	19.73	Cell 12	66.925
Cell 3	34.145	Cell 13	70.04
Cell 4	46.79	Cell 14	73.895
Cell 5	58.505	Cell 15	78.32
Cell 6	68.555	Cell 16	82.65
Cell 7	76.84	Cell 17	87.095
Cell 8	84.135	Cell 18	91.35
Cell 9	89.555	Cell 19	94.715
Cell 10	94.445	Cell 20	98.535

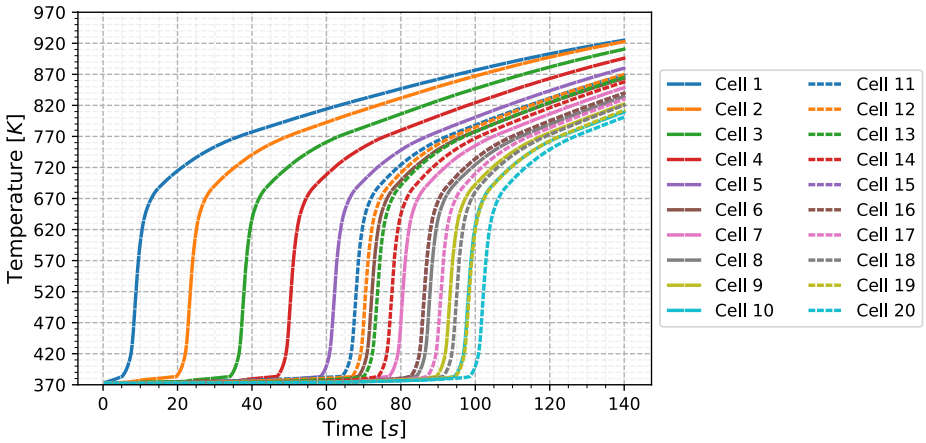

Figure 4.18: Volume average temperature of battery cells with reduced foam thermal conductivity.

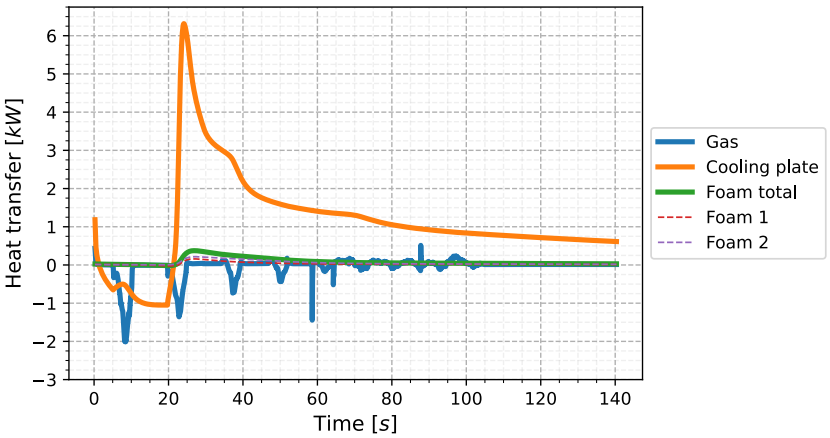

Figure 4.19: Heat transfer out of cell 2 with reduced foam thermal conductivity.

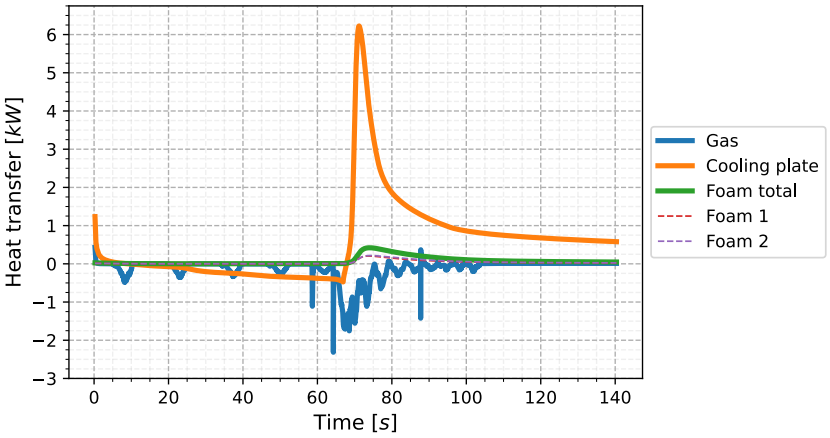

Figure 4.20: Heat transfer out of cell 12 with reduced foam thermal conductivity.

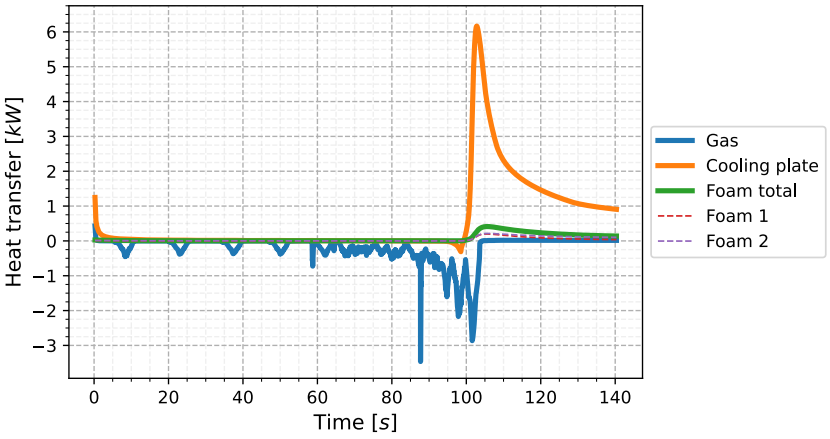

Figure 4.21: Heat transfer out of cell 20 with reduced foam thermal conductivity.

4.6 Comparing cases

With the results from the different cases presented they can now be compared. The times of thermal runaway for the different cases are compared in figure 4.22 in which time of TR is plotted for each cell number. The battery cells that are connected in series have lines connecting them to signify this. By integrating the heat transfer data used to create figures 4.11-4.13, 4.15-4.17 and 4.19-4.21 the total amount of energy going out of the battery cells during different time periods can be obtained. The integration is split into two time periods. One period is defined from zero seconds to the time of TR for the cell. The other period is defined from the time of TR for the cell to the time of TR for the last cell to enter TR plus 30 seconds. Figures 4.23, 4.24 and 4.25 show the total amount of energy going out of the battery cells into the gas, foam and cooling plate before the onset of TR respectively. In figure 4.26 the values in the previous three figures are combined giving the total amount of energy going into each battery cell before TR. The battery cells that are connected in series have lines connecting them here as well. A negative value means that the battery cell is receiving energy from the surroundings through heat transfer. Similarly figures 4.27, 4.28, 4.29 and 4.30 show the same thing as described above but after TR in each cell.

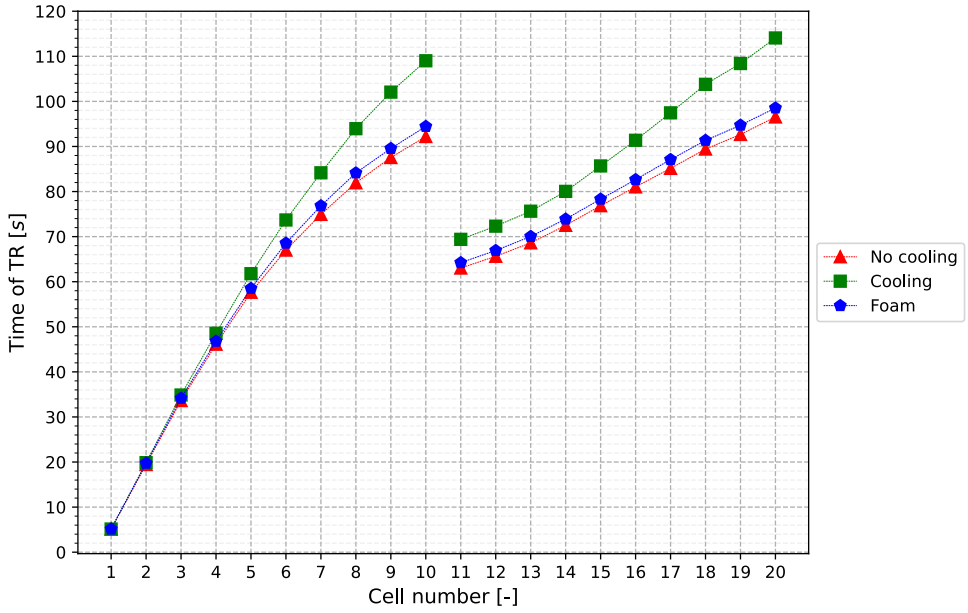

Figure 4.22: Comparison of thermal runaway times for every cell between the different cases.

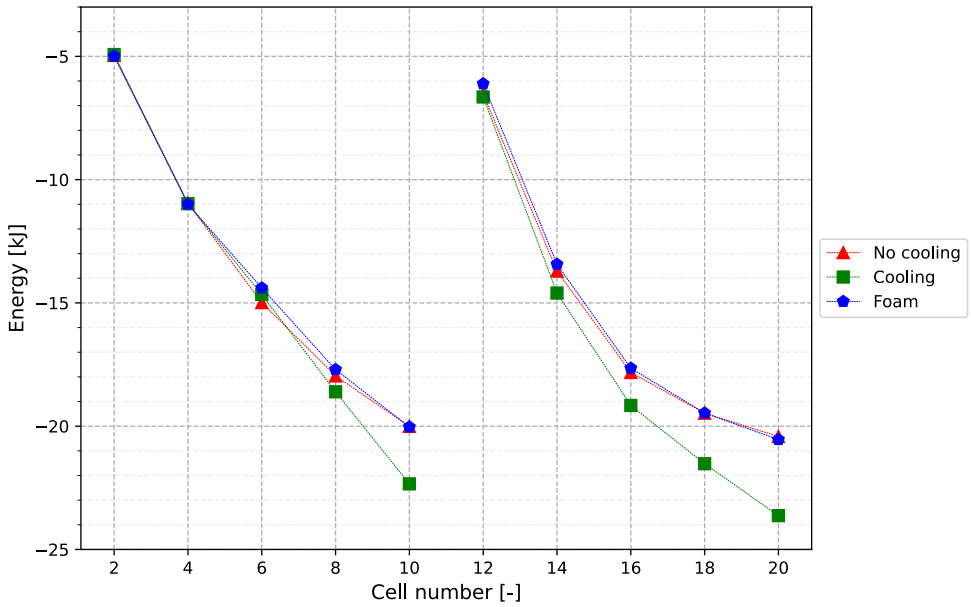

Figure 4.23: Comparison of the amount of energy going out of the battery cells to the gas before the cells go into TR.

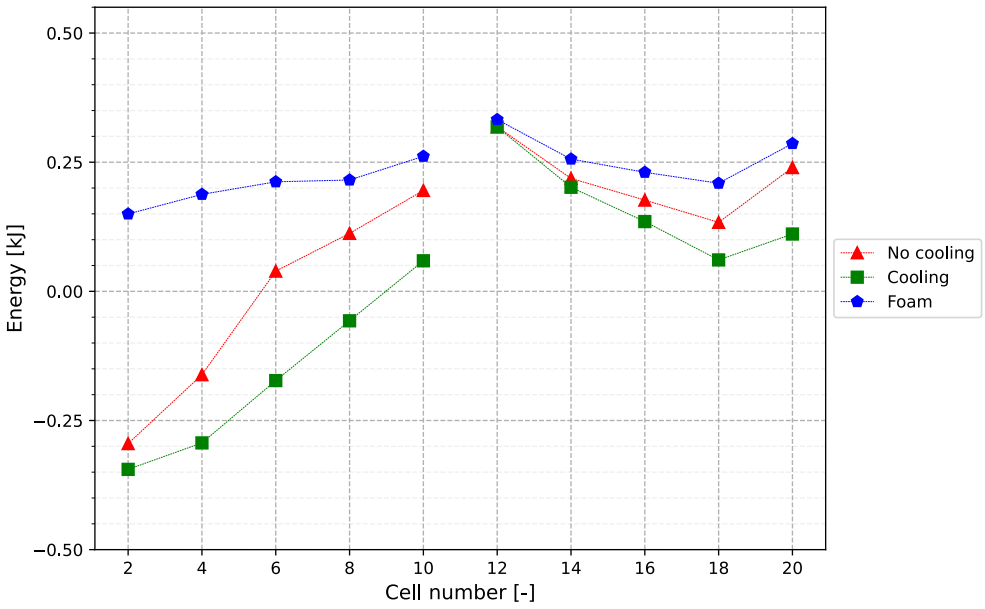

Figure 4.24: Comparison of the amount of energy going out of the battery cells to the foam before the cells go into TR.

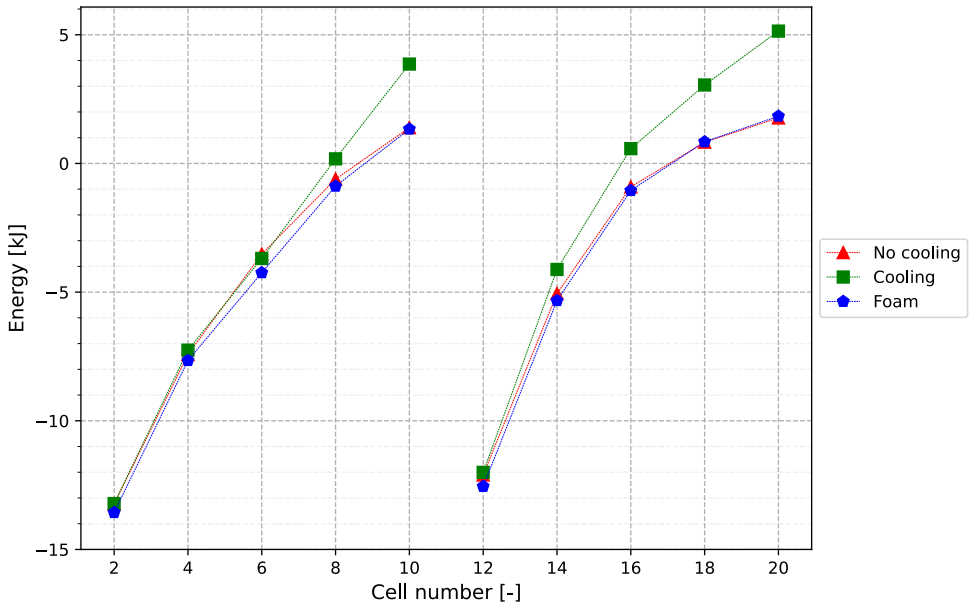

Figure 4.25: Comparison of the amount of energy going out of the battery cells to the cooling plate before the cells go into TR.

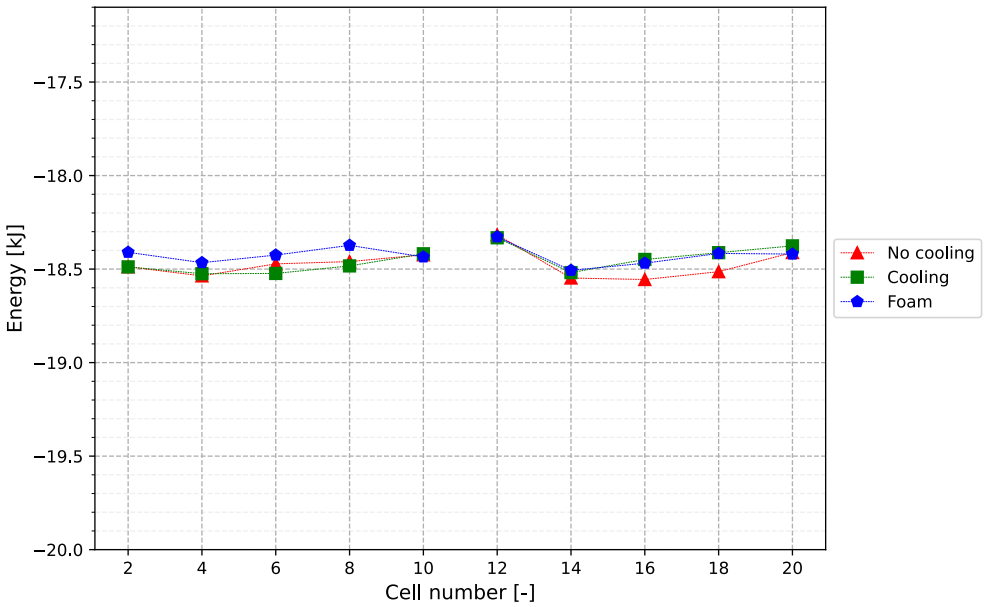

Figure 4.26: Comparison of the total amount of energy going out of the battery cells before the cells go into TR.

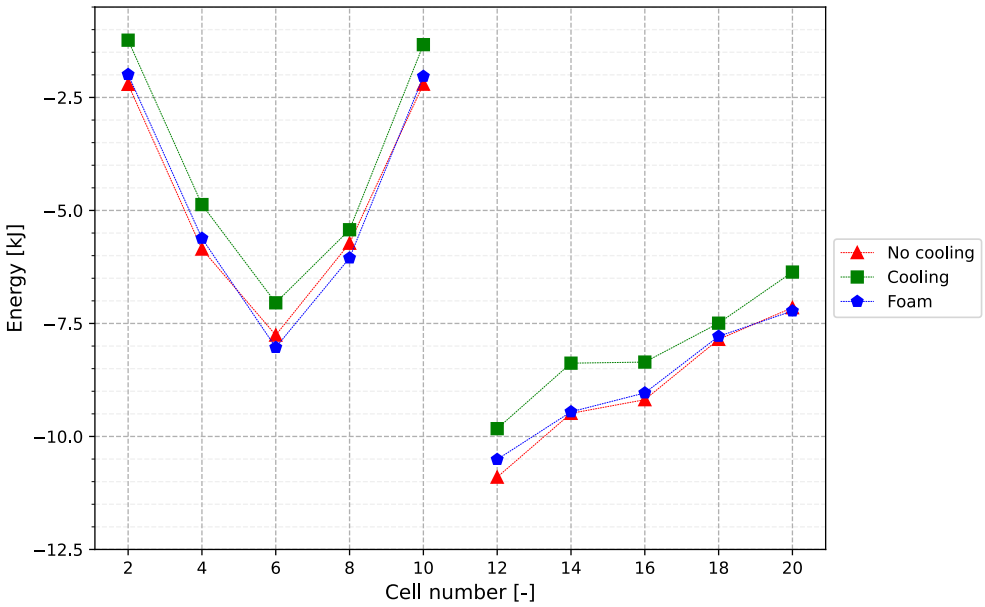

Figure 4.27: Comparison of the amount of energy going out of the battery cells to the gas after the cells go into TR.

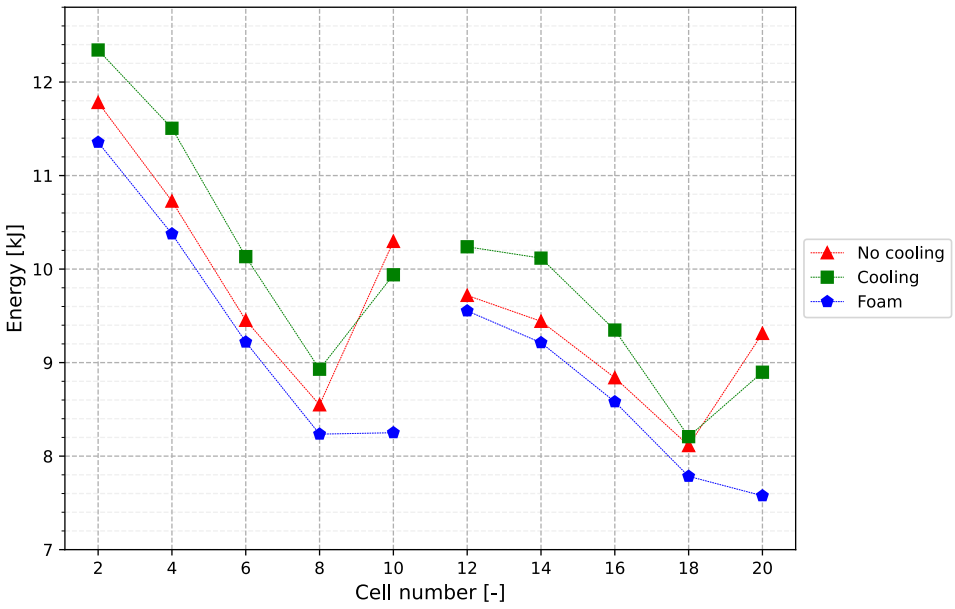

Figure 4.28: Comparison of the amount of energy going out of the battery cells to the foam after the cells go into TR.

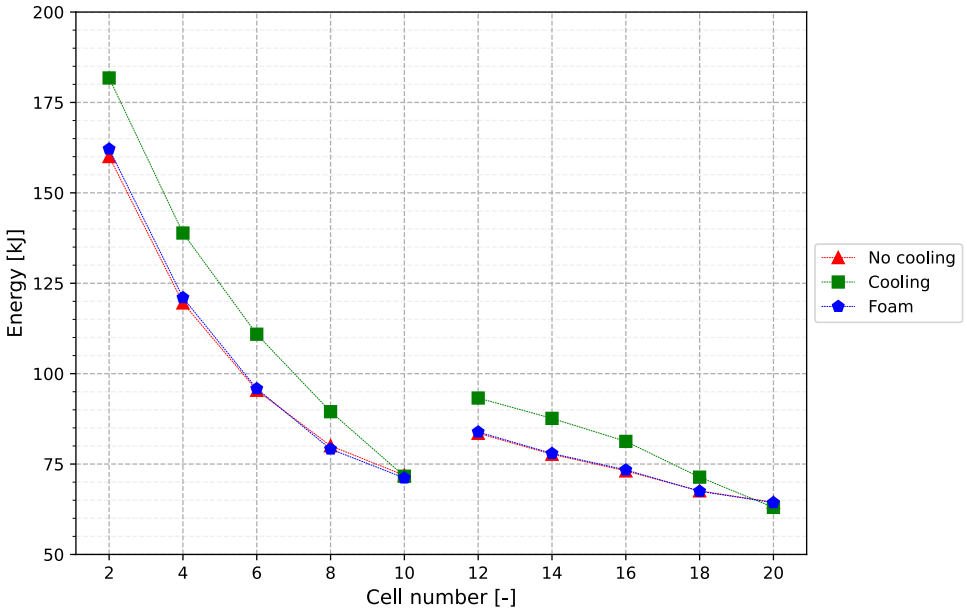

Figure 4.29: Comparison of the amount of energy going out of the battery cells to the cooling plate after the cells go into TR.

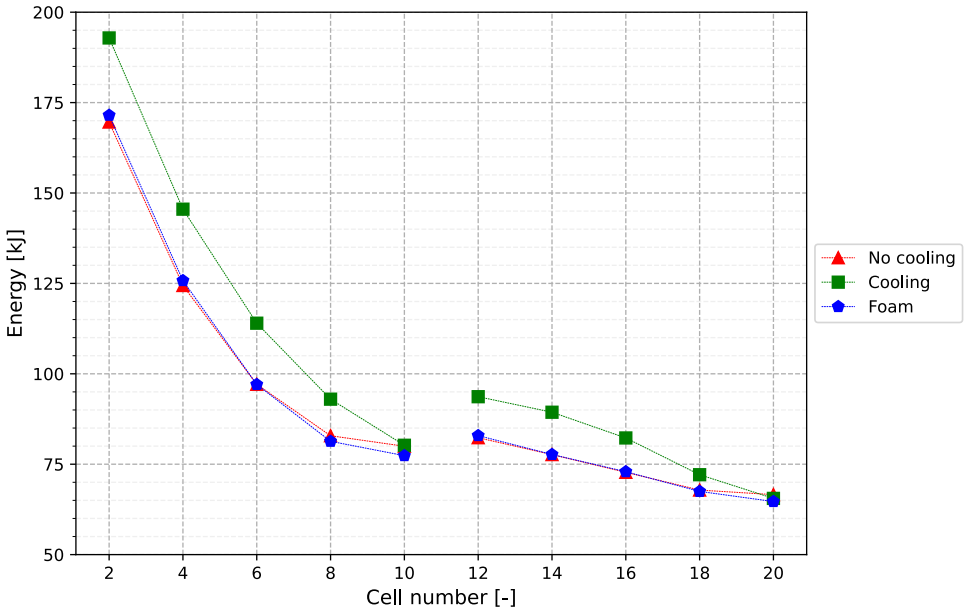

Figure 4.30: Comparison of the total amount of energy going out of the battery cells after the cells go into TR.

5
Discussion

In chapter the results from the previous chapter are discussed so that relevant conclusion can be drawn. First the results from the mesh independence study and comparison of turbulence models are discussed. After that the models used to simulate thermal runaway are evaluated and finally trends observed in the different cases are discussed.

5.1 Mesh independence study

In this thesis a variation in results between meshes less than 1% was chosen to be the criteria for an independent mesh. Looking at the results in section 4.1 we see that the variation of trigger time for TR differs by less than 1% between the base and fine mesh. As for the heat transfer the convergence is not as good. The heat transfer to the cooling plate and foam differs less than 0.3% between the base and fine mesh but the heat transfer to the gas differs by 4.78%. The base mesh can therefore be said to be independent in all aspects except for heat transfer to gas. The aim of this thesis is to predict trigger times of TR and since that aspect of the base mesh is independent it is deemed sufficiently good to use.

5.2 Effect of turbulence model

The same independence criteria of 1% as in the mesh independence study is used here to compare the turbulence models. Looking at table 4.2 we see that the heat transfer to the solids is almost the same for both cases which is expected because the turbulence model does not affect conduction in solids. For the same reason the time of TR in cell 2 is also very similar in both cases. What separates the results from the turbulence models is how much heat is transferred to the gas which in turn affects the time of TR in cells 3 and 4. With the $k-\omega$ SST model more heat is transferred to the gas leading to higher temperatures in the module which makes the surface of the cells heat up faster, leading to TR earlier than with the $k-\varepsilon$ model.
The figures visualizing the flow differ between the $k-\omega$ SST and $k-\varepsilon$ models. In the vector velocity field, figures 4.3 and 4.4, we see larger recirculation regions with $k-\omega$ SST and along the cell surface we see an additional recirculation region that does not appear when using the $k-\varepsilon$ model. As for the streamlines in figures 4.5 and 4.6 the models produce similar results at large but the $k-\varepsilon$ model produces

streamlines that look more chaotic whereas the $k-\omega$ SST model produces more orderly looking streamlines.
We see in table 4.2 that the percentage difference between the models is larger than the criteria of 1% for three of the seven total compared metrics but is larger than 1% in all metrics that have to to with heat transfer to and from the gas. Therefore we can say that the simulation is turbulence model dependent.
Knowing which turbulence model is the most correct is not possible to say without validation data, however the theory provides some input as to which model is more appropriate. The $k-\omega$ SST model should be more accurate close to walls than the $k-\varepsilon$ model meaning that it more accurately predicts heat transfer and therefore time of TR as well.

5.3 Model evaluation

Looking at figures 4.8 and 4.9 which show the mass flow from the venting inlets of the battery cells and the total temperature of these inlets we see that they match table 3.1 exactly. The velocity from the vents in figure 4.10 follow the ideal gas law and are close to initial guesses used to predict the Reynolds number in the y^+ calculations in section 3.4.2. We see that the peak velocity after each TR is different. Since the mass flow and total temperature are identical for each TR this must be due to the composition of gases and pressure inside of the case. A higher pressure will push back against the vented gases leading to lower velocities and vice versa. A higher concentration of air will also limit the velocity because it has a lower gas constant, R, while a higher concentration of vented gases will lead to higher velocities of the vented gas because the gas constant of the vented gases is higher.
The volume average temperature in figures 4.7, 4.14 and 4.18 follows table 3.4. We see that at about 620 K the rate of heating starts to decrease, in according to the table.

5.4 Trends

We can find some trends by looking at the results. Figure 4.22 shows a comparison of thermal runaway times between the cases. We see that the order in which cells go into TR is the exact same between cases except for the cooling case where cell 10 goes into TR before cell 19, while the opposite is true for the other cases. The first row of cells (1-10) starts the thermal runaway of the module and it takes over a full minute until the first cell of the second row (11-20) enters TR. When the second row has entered TR the spread of TR accelerates and it only takes about 35-45 s until the last cell has entered TR. It then follows that the second row of cells has a lower average time between TR than the first row for all three cases. This demonstrates the accelerating nature of thermal runaway.
When it comes to the different cases it can be clearly seen that cooling has a larger impact on delaying TR than better insulating foam. We also see that the cooling makes a bigger difference the further along each row the TR propagates. The better insulating foam has a similar effect in the first row of cells as the difference increases

but in the second row the difference is almost constant.
The different cases can be compared further by looking at the energy transport to and from the battery cells.

5.4.1 Before thermal runaway

It can be observed through figure 4.26 that the almost the same net amount of energy is transported into each battery cell before each of them enter TR. The average amount of energy transported into the cells is largest for the case without cooling and smallest for the case with better insulating foam. However, the difference is only 50 J.
Looking at where this transported energy comes from shows some interesting things. Firstly we see in figure 4.24 that not much energy at all is transported from or goes into the foam. In the two cases with the regular foam there are two and four data points where energy is transported into the battery cells from the foam. For all other probed cells energy is transported out of the battery cells into the foam. In the case with improved foam energy is transported out of the battery cells into the foam. We can also see that introducing cooling decreases the amount of energy transported into the foam because in that case the energy transport into the cooling plate is increased.
Secondly by looking at figure 4.23 we see that battery cells have more energy transported into them from the gas the later they enter TR. This is because cells that enter TR later have been exposed to more vented gases. It can also be observed that in the cooling case more energy is transported into the battery cells from the gas than for the other cases.
Thirdly in figure 4.25 we see that battery cells that enter TR later transport energy into the cooling plate. The reason for this is due to the initial conditions. The cooling plate is initialized to be 10 K colder than the battery cells. This leads to heat transfer from the battery cells to the cooling plate. This effect is inflated in the case with cooling because the temperature of the cooling plate is decreased further, increasing the temperature gradient and the rate of heat transfer according to Fourier's law (2.11). The heat transfer to the cooling plate is so slow that in most of the battery cells the energy transport to the cooling plate is negative due to heat from TR spreading through the cooling plate to the neighboring cells.

5.4.2 After thermal runaway

If we start by looking at figure 4.28 we see that the cells that go into TR early transport more energy into the foam after TR due to a larger time period being used in the integration for the earlier cells. The case with the improved insulation decreases the amount of energy transported into the foam while the case with cooling increases it.
As for the gas we see in figure 4.27 that the energy transport out of the battery cells is negative, meaning the gas is transporting energy into the cells. Similar to the foam wee see that the second row of cells have more energy transported into them from the gas the earlier the cells go into TR due to the time periods used in the

integration. The behaviour of the first row is not as easily explained.
We would expect a similar shape in the graph as for the second row but instead we see a kind of "v"-shape for the first row of cells. A possible explanation for this can be found by looking at the times of TR in figure 4.22 as well as the volume average temperatures in figures 4.7, 4.14 and 4.18.
The first part of the explanation is found by looking at the figures for volume average temperature which show that within 15 s after TR the battery cell reaches 710 K. This temperature is so high that the temperature gradient to the gas becomes small and heat transfer becomes limited. If we then look at the times of TR we see that within 15 s after TR in cells 2 and 4 none or one cell go into TR while for cells 6 and 8 five cells go into TR. Cell 10 goes into TR last or second to last so it has one or two cells that go into TR after it. This means that cells 6 and 8 have much energy transported into them from the gas before they reach a high average temperature.
Time, just like for the foam, explains the other half. Cells 2 and 4 go into TR early and have time to reach a high volume average temperature which can be seen in the figures. The high average temperature enables energy to be transported from the battery cells to the gas. They also experience the venting of hot gas from all the other cells which is why the values are negative. Cells 6 and 8 receive a large amount of energy transported from the gas. Finally cell 10 receives a little energy transported from the gas and does not have time to reach a high temperature in order to transfer heat to the gas.
Looking at figure 4.29 we see a clear connection to time of TR. The earlier the battery cell went into TR the more heat it has transferred into the cooling plate. It is also observed that the amount of energy transported into the cooling plate is many times larger than into the other parts. This leads to figure 4.30, which shows the total amount of energy transported from the battery cells, looking almost the same. Due to the times of TR being delayed in the cooling case the battery cells have more time to transfer heat leading to more energy being transported from them. We also see that that the difference in amount of energy transported between the cases decreases in the order that the cells entered TR.
The case with cooling increases the energy transported into gas, foam and cooling plate. This is because cooling increases conduction by creating a larger temperature gradient.

6
Conclusion

In this thesis the aim was to predict propagation time between battery cells and implementing different strategies to delay the spread of TR within the battery module. This was achieved with the models used.
It was found that the turbulence model used had an effect on the results obtained. The different cases tested provided different insight both into the propagation time of TR as well as how heat is transferred both before and after TR is triggered in the cells. Implementing cooling was more efficient than improving the insulating properties of the foam and its positive effect on propagation time increased in a non-linear way as TR spread in the module.
It was observed that heat spread from neighboring cell to neighboring cell through the cooling plate while heat from the vented gases transferred to all cells, increasing their temperature. The vented gases then effectively lower the threshold that the heat that spreads through the cooling plate has to overcome to trigger cells into TR which accelerates the spread of TR in the module the more cells are triggered.
From these observations strategies to further mitigate and slow the propagation of TR within a battery module can be thought of. One idea is to limit the heat transfer through the cooling plate by dividing it into many smaller cooling plates that are thermally insulated from each other. One for each battery cell would be most effective in terms of delaying TR but practically inefficient as it would make manufacturing more complex and hence more expensive. Another idea is to improve the ventilation of the battery module such that the vented gases are removed quickly and the temperature within the module is lower. This would require some sort of fan system which would add size and weight to the battery pack.

6.1 Future scope

Further work can be done to obtain more accurate results for a smaller computational cost.
Firstly the mesh process could be improved in one of two different ways. One option is to generate a fully conformal mesh in order to obtain more accurate heat transfer results because the faces on interfaces match one-to-one. The other option is to coarsen the mesh of the solid parts when using the non-conformal mapped interfaces as the mesh on both sides of the interface can be of different size without any problems. This would reduce computational time by reducing the overall cell count without sacrificing accuracy.
Secondly a time step independence study similar to the mesh independence study

could be conducted to find out if the time step used in this thesis is fine enough to predict thermal runaway propagation accurately. The time step could also be optimized for example by being refined more when the velocity in the vented gas is at its highest.
Thirdly the complexity of the model could be increased to include the internal chemistry of the battery cells to simulate the heat released during TR in a different and perhaps accurate way. Phase changes could also be included as the foam likely would melt in reality. The effects of radiation would be interesting to include to see how it affects propagation time.
Fourthly having access to validation data from the same or similar cases would give definitive answers to questions regarding how accurate the models used are and for example which turbulence model to use for this application. If data from experiments is too expensive or difficult to acquire results from 1D simulations could be used.
Lastly a newer version of the software could be used. In this theses Simcenter Star-CCM+ version 2306 (June 2023 release) was used due to license limitations. In version 2310 the thermal runway battery model was expanded in Star-CCM+ to include a built in model for battery venting as well as changing the battery density during venting. Using this version in the future would simplify the set-up substantially by removing the need to specify the venting though the use of reports and complicated expressions.

Bibliography

[1] L. Davidson. *Fluid mechanics, turbulent flow and turbulence modeling*. Chalmers University of Technology, 2024. URL: https://www.tfd.chalmers.se/~lada/postscript_files/solids-and-fluids_turbulent-flow_turbulence-modelling.pdf.

[2] J. P. Holman. *Heat Transfer*. 10th ed. New York, NY: McGraw-Hill Education, 2010. ISBN: 978-0-07-352936-3.

[3] X. Hu et al. "Advancements in the safety of Lithium-Ion Battery: The Trigger, consequence and mitigation method of thermal runaway". In: *Chemical Engineering Journal* 481 (2024), p. 148450. ISSN: 1385-8947. DOI: https://doi.org/10.1016/j.cej.2023.148450. URL: https://www.sciencedirect.com/science/article/pii/S1385894723071826.

[4] U. R. Institutes. *What Are Lithium-Ion Batteries?* 2021. URL: https://ul.org/research/electrochemical-safety/getting-started-electrochemical-safety/what-are-lithium-ion.

[5] P.-A. Le et al. "Overview of the Thermal Runaway in Lithium-Ion Batteries with Application in Electric Vehicles: Working Principles, Early Warning, and Future Outlooks". In: *Energy & Fuels* 37.22 (2023), pp. 17052–17074. DOI: 10.1021/acs.energyfuels.3c02548. URL: https://doi.org/10.1021/acs.energyfuels.3c02548.

[6] Matweb. *Overview of materials for Thermoset Polyurethane Foam, Unreinforced*. 2024. URL: https://www.matweb.com/search/DataSheet.aspx?MatGUID=91d44cae736e4b36bcba94720654eeae&ckck=1.

[7] S. Shahid and M. Agelin-Chaab. "A review of thermal runaway prevention and mitigation strategies for lithium-ion batteries". In: *Energy Conversion and Management: X* 16 (2022), p. 100310. ISSN: 2590-1745. DOI: https://doi.org/10.1016/j.ecmx.2022.100310. URL: https://www.sciencedirect.com/science/article/pii/S2590174522001337.

[8] H. K. Versteeg and W. Malalasekera. *An Introduction to Computational Fluid Dynamics*. 2nd ed. Pearson Education Limited, 2007.

[9] J. T. Warner. *Lithium-Ion Battery Chemistries*. Elsevier, 2019. ISBN: 978-0-12-814778-8. DOI: https://doi.org/10.1016/C2017-0-02140-7. URL: https://www.sciencedirect.com/book/9780128147788/lithium-ion-battery-chemistries.

[10] F. M. White. *Fluid mechanics*. 8th ed. New York, NY: McGraw-Hill Education, 2016. ISBN: 978-0-07-352934-9.

A

Appendix 1

A.1 No cooling

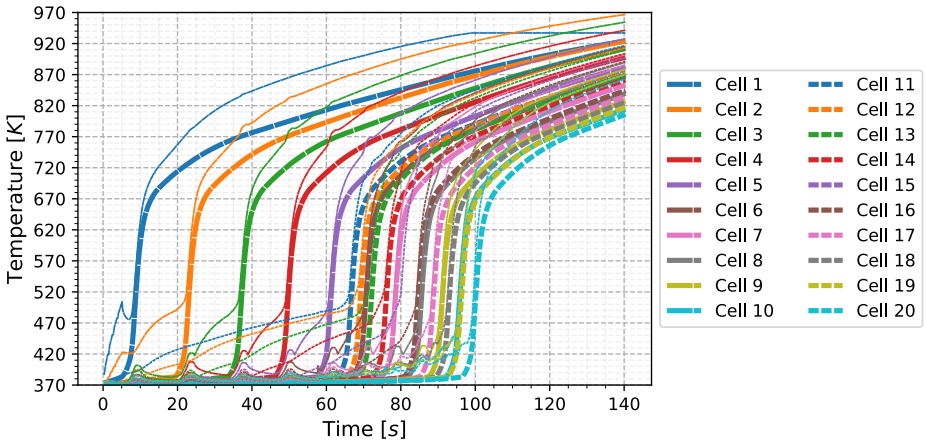

Figure A.1: Volume average temperature and maximum temperature of battery cells with no cooling implemented. Thin lines are maximum temperature.

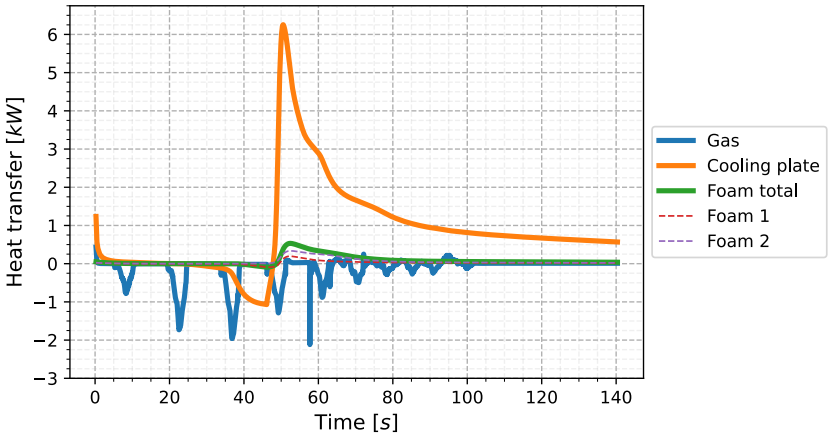

Figure A.2: Heat transfer out of cell 4 with no cooling implemented.

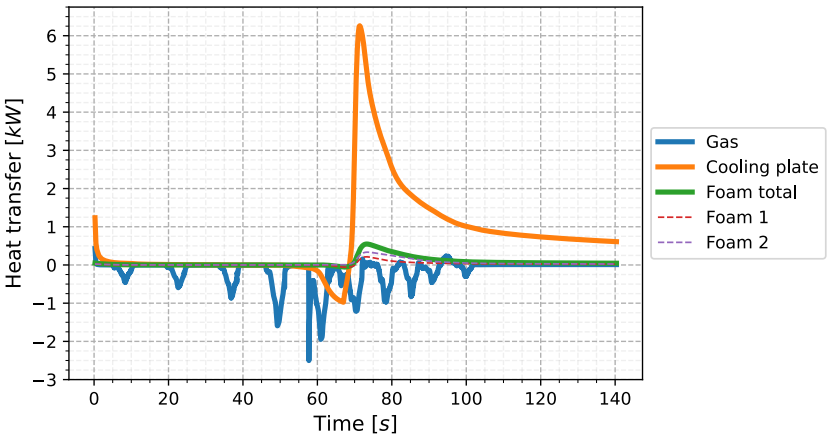

Figure A.3: Heat transfer out of cell 6 with no cooling implemented.

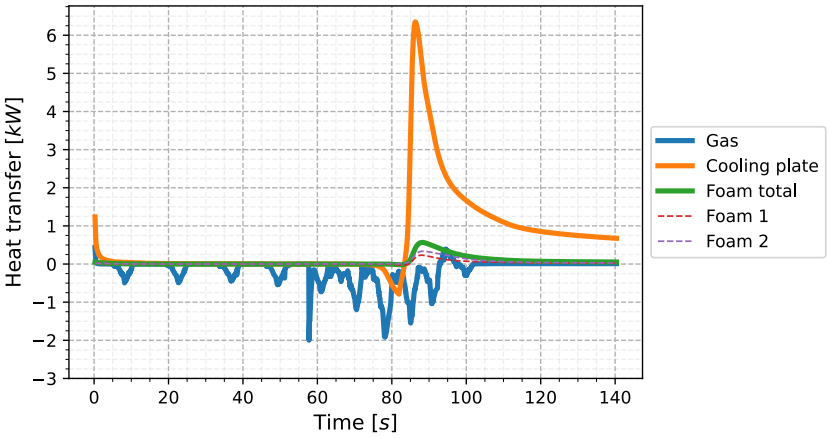

Figure A.4: Heat transfer out of cell 8 with no cooling implemented.

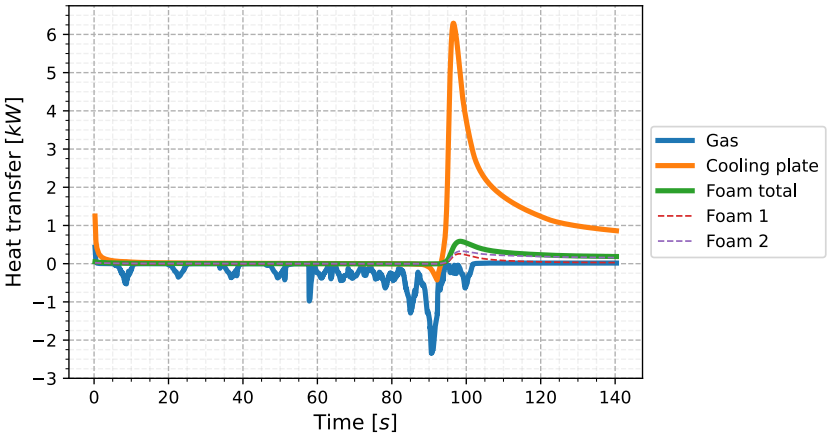

Figure A.5: Heat transfer out of cell 10 with no cooling implemented.

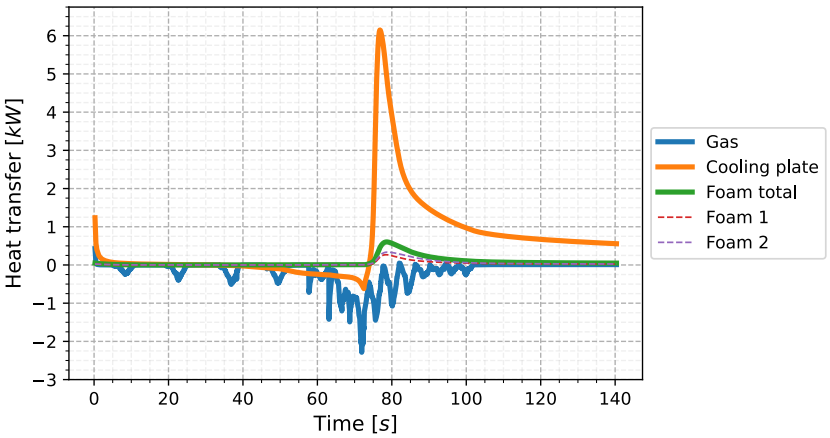

Figure A.6: Heat transfer out of cell 14 with no cooling implemented.

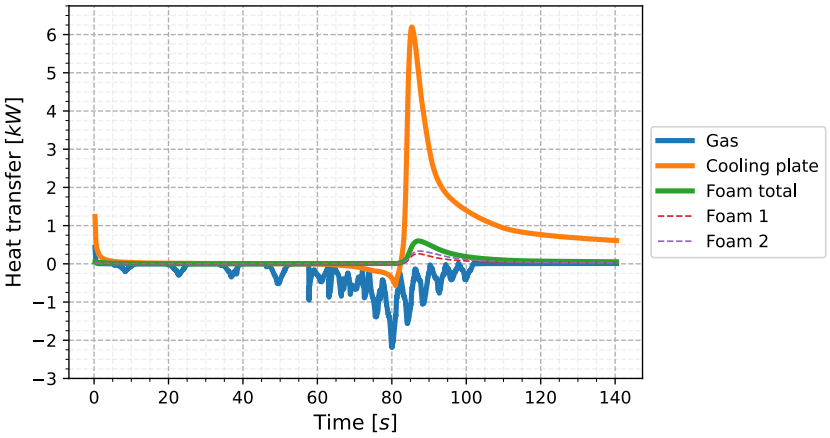

Figure A.7: Heat transfer out of cell 16 with no cooling implemented.

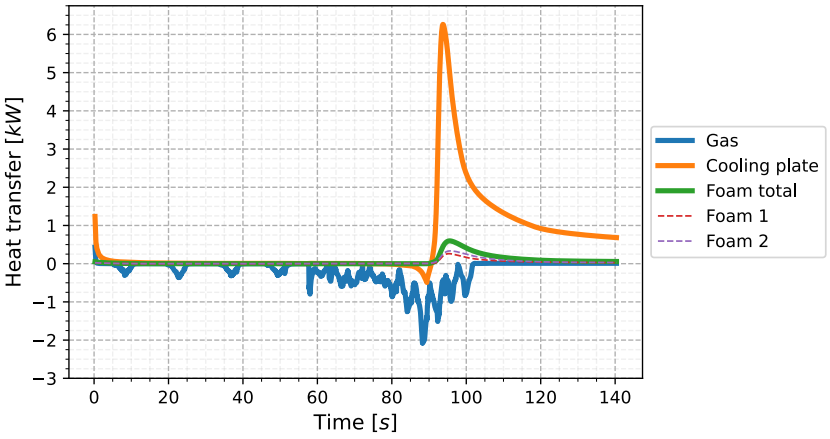

Figure A.8: Heat transfer out of cell 18 with no cooling implemented.

A.2 Cooling

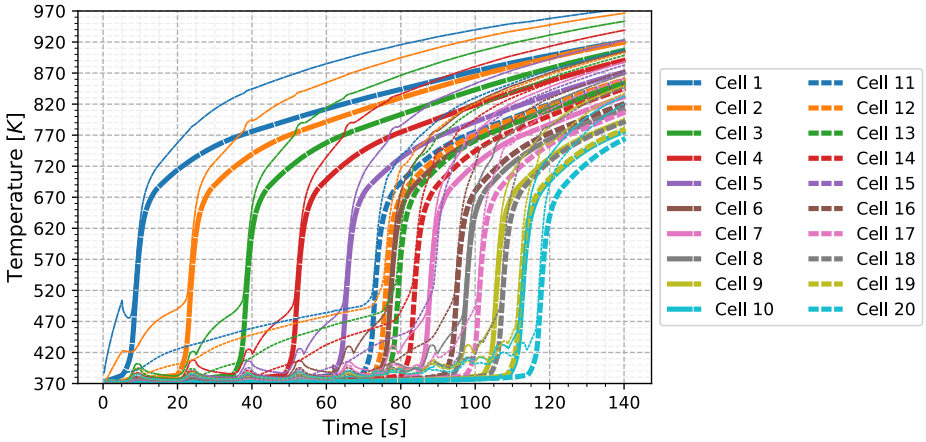

Figure A.9: Volume average temperature and maximum temperature of battery cells with cooling implemented. Thin lines are maximum temperature.

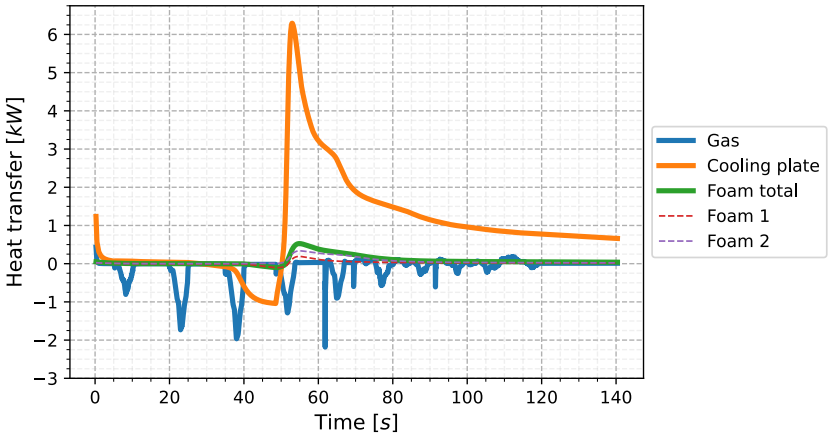

Figure A.10: Heat transfer out of cell 4 with cooling implemented.

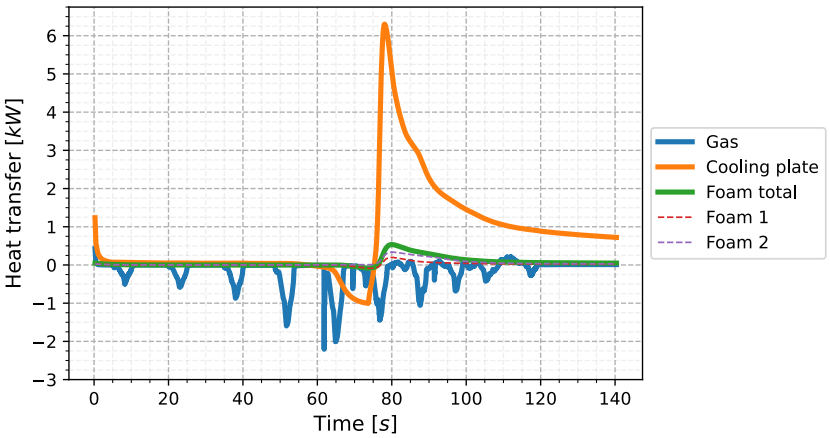

Figure A.11: Heat transfer out of cell 6 with cooling implemented.

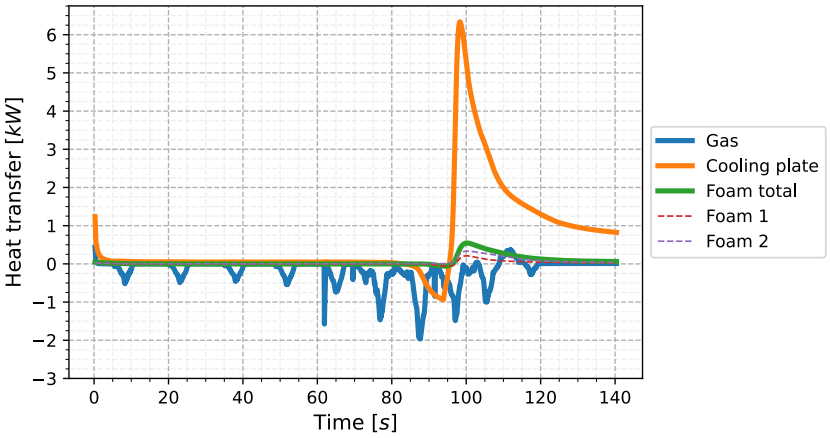

Figure A.12: Heat transfer out of cell 8 with cooling implemented.

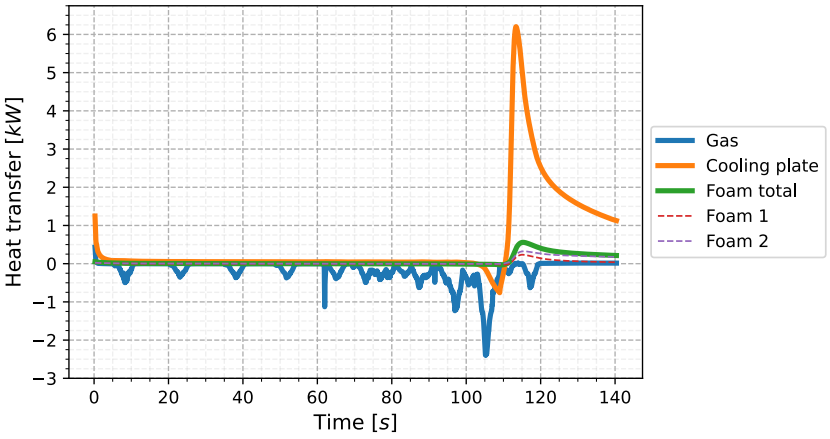

Figure A.13: Heat transfer out of cell 10 with cooling implemented.

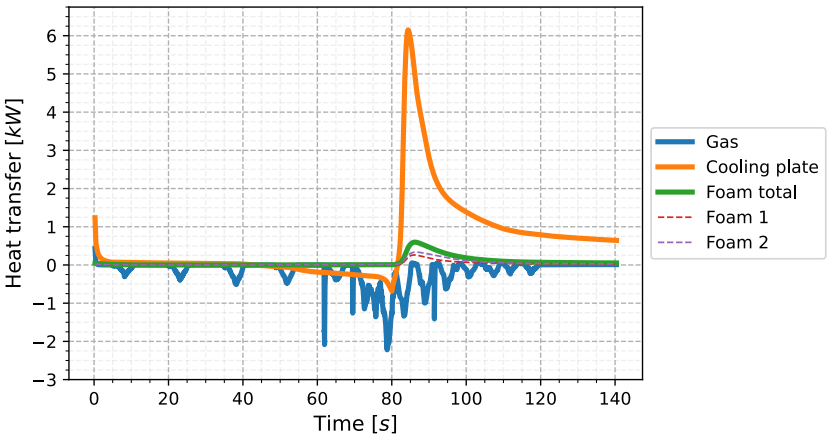

Figure A.14: Heat transfer out of cell 14 with cooling implemented.

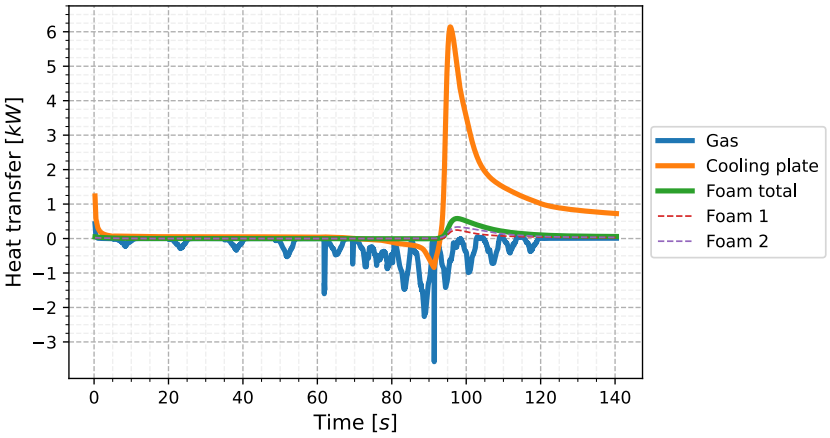

Figure A.15: Heat transfer out of cell 16 with cooling implemented.

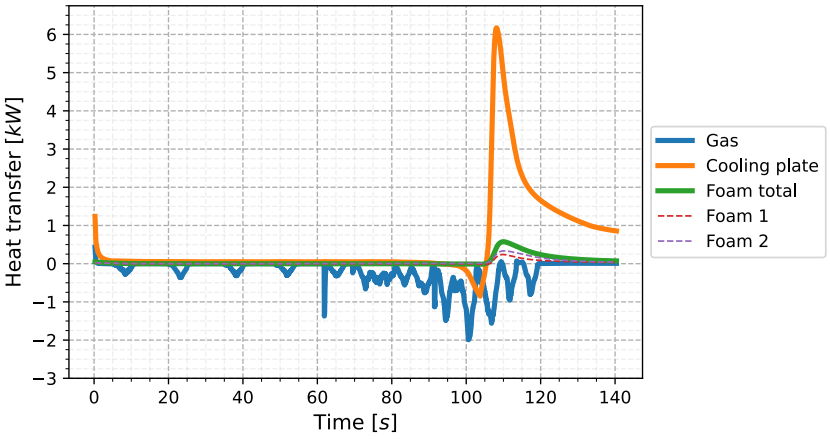

Figure A.16: Heat transfer out of cell 18 with cooling implemented.

A.3 Reduced foam thermal conductivity

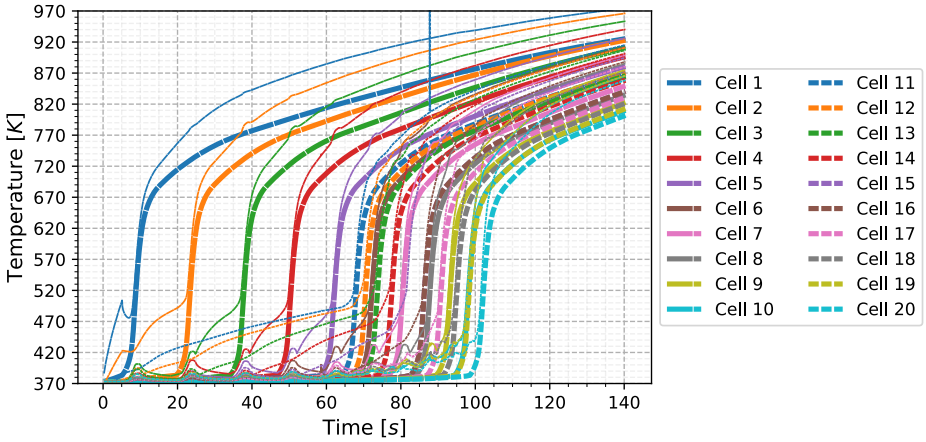

Figure A.17: Volume average temperature and maximum temperature of battery cells with reduced foam thermal conductivity. Thin lines are maximum temperature.

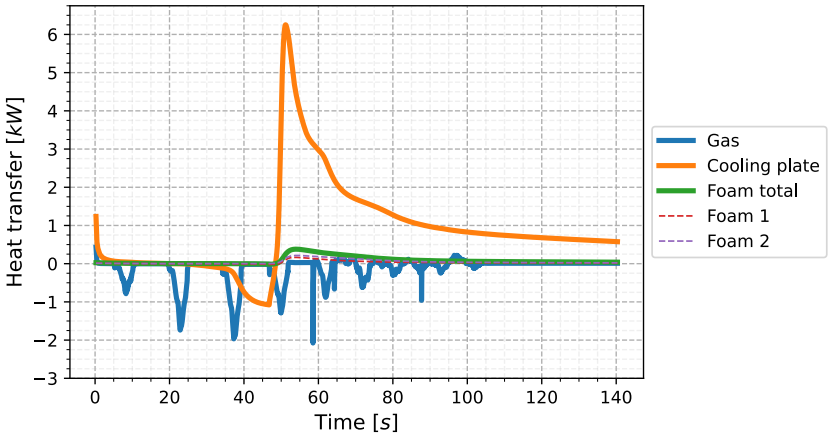

Figure A.18: Heat transfer out of cell 4 with reduced foam thermal conductivity.

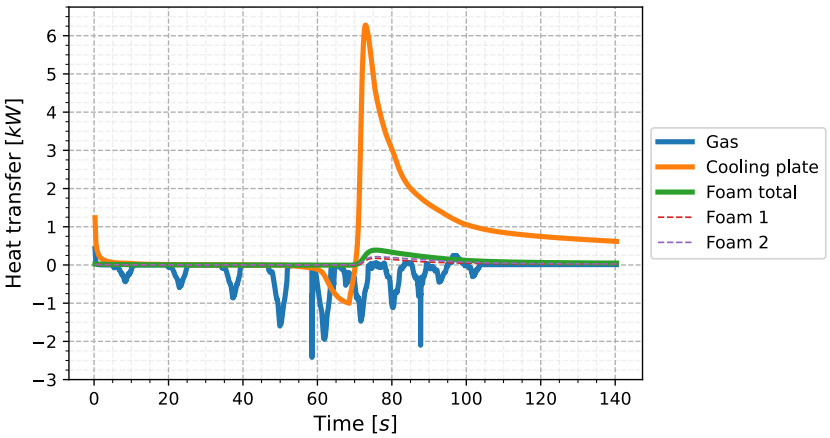

Figure A.19: Heat transfer out of cell 6 with reduced foam thermal conductivity.

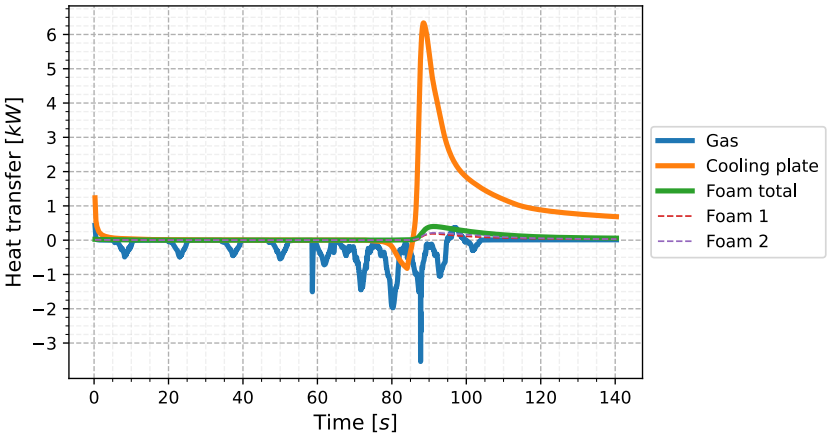

Figure A.20: Heat transfer out of cell 8 with reduced foam thermal conductivity.

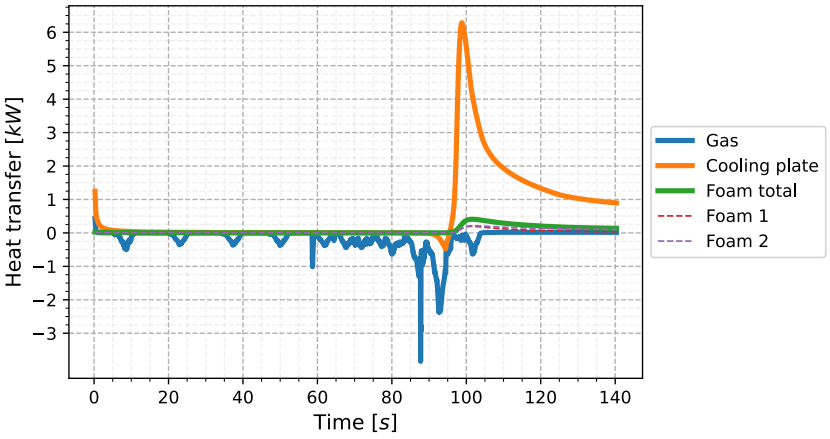

Figure A.21: Heat transfer out of cell 10 with reduced foam thermal conductivity.

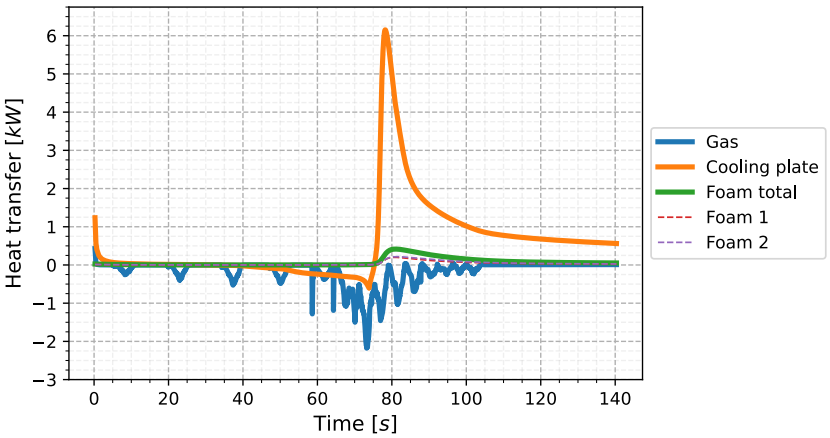

Figure A.22: Heat transfer out of cell 14 with reduced foam thermal conductivity.

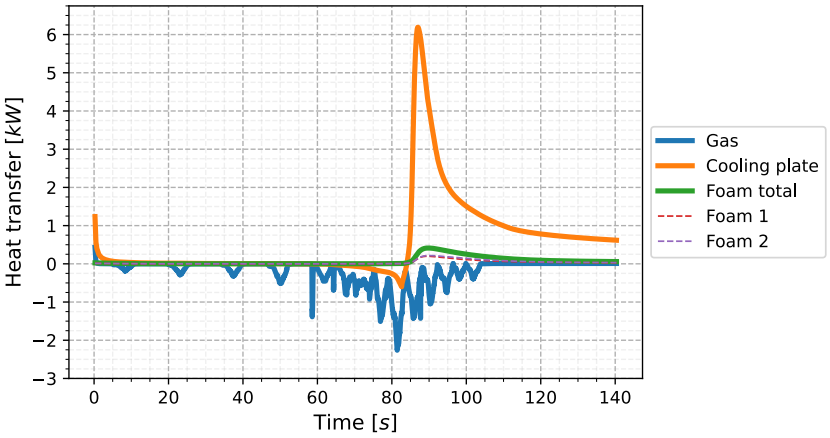

Figure A.23: Heat transfer out of cell 16 with reduced foam thermal conductivity.

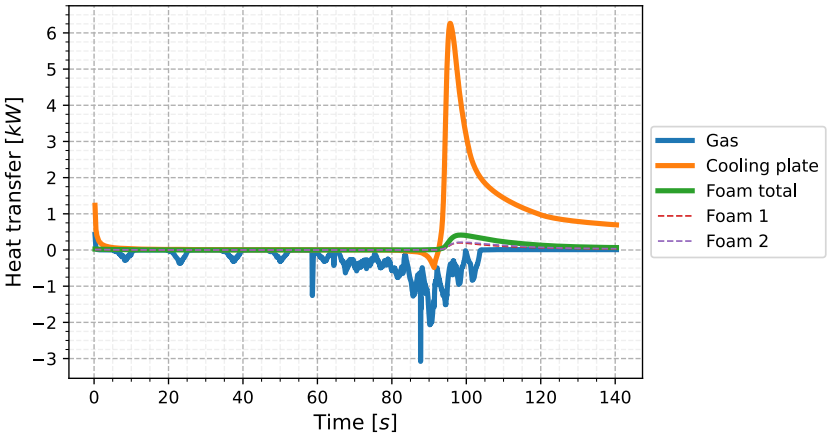

Figure A.24: Heat transfer out of cell 18 with reduced foam thermal conductivity.

DEPARTMENT OF MECHANICS AND MARITIME SCIENCES
CHALMERS UNIVERSITY OF TECHNOLOGY
Gothenburg, Sweden
www.chalmers.se

CHALMERS
UNIVERSITY OF TECHNOLOGY